

# A contact model for sticking of adhesive mesoscopic particles

A. Singh, V. Magnanimo and S. Luding

Multi Scale Mechanics, CTW, MESA+, UTwente,

P.O.Box 217, 7500 AE Enschede, Netherlands,

e-mail: a.singh-1@utwente.nl, v.magnanimo@utwente.nl, s.luding@utwente.nl

## Abstract

The interaction between realistic visco-elasto-plastic and adhesive meso-particles is the subject of this study. The final goal is to define a simple, flexible and useful interaction model that allows to describe the multi-contact bulk behavior of assemblies of non-homogeneous/non-spherical particles, e.g. with internal structures of the scale of their contact deformation. We attempt to categorize previous approaches and propose a simplified mesoscale normal contact model that contains the essential ingredients to describe an ensemble of particles, while it is not aimed to include all details of every single contact, i.e. the mechanics of constituent elementary, primary particles is not explicitly taken into account.

The model combines short-ranged, non-contact adhesive interactions with an elaborate, piece-wise linear visco-elasto-plastic adhesive contact law. Using energy conservation arguments, the special case of binary collisions is studied and an analytical expression for the coefficient of restitution in terms of impact velocity is derived. The assemblies (particles or meso-particles) stick to each other at very low impact velocity, while they rebound less dissipatively with increasing velocity, in agreement with experimental/theoretical/numerical findings for elasto-plastic spherical particles. For larger impact velocities we observe an interesting second sticking regime. While the first sticking is attributed to dominating non-contact adhesive forces, while the high velocity sticking is due to a balance

between the non-linearly increasing history dependent adhesion and plastic dissipation. The model allows for a stiff, elastic core material, which produces a new rebound regime at even higher velocities.

The relevance of the model for various types of bulk materials is critically discussed with respect to features as: non-linear pressure dependent bulk stiffness, limit elasticity vs plasticity or non-perfect detachment under slow tension.

**Keywords: Meso-scale, Particle collision, Sticking, Cohesive material, Elastoplastic material, Core-shell materials**



## Nomenclature

$m_i$	: mass of $i^{th}$ particle.
$a_i$	: Radius of $i^{th}$ particle.
$m_r$	: Reduced mass of two particles.
$\delta$	: Contact overlap between particles.
$k$	: Spring stiffness.
$v_i$	: Relative velocity before collision.
$v_f$	: Relative velocity after collision.
$v_i^\infty$	: Relative velocity before collision at infinite separation.
$v_f^\infty$	: Relative velocity after collision at infinite separation.
$v^n$	: Normal component of relative velocity.
$e$	: Coefficient of restitution.
$\varepsilon_i$	: Pull-in coefficient of restitution.
$e_n$	: Normal coefficient of restitution.
$\varepsilon_o$	: Pull-off coefficient of restitution.
$k_1$	: Slope of loading plastic branch.
$k_2$	: Slope of unloading and re-loading elastic branch.
$k_p$	: Slope of unloading and re-loading limit elastic branch.
$k_c$	: Slope of irreversible, tensile adhesive branch.
$v_p$	: Relative velocity before collision for which the limit case of overlap is reached.
$\phi_f$	: Dimensionless plasticity depth.
$\delta_{\max}$	: Maximum overlap between particles for a collision.
$\delta_{\max}^p$	: Maximum overlap between particles for the limit case.
$\delta_0$	: Force free overlap $\cong$ plastic contact deformation.
$\delta_{\min}$	: Overlap between particles at the maximum negative attractive force.
$\delta_c$	: Kinetic Energy free overlap between particles.
$W_{\text{diss}}$	: Amount of energy dissipated during collision.
$\eta$	: Dimensionless plasticity of the contact.
$\beta$	: Adhesivity: dimensionless adhesive strength of the contact.
$\chi$	: Scaled initial velocity relative to $v_p$ .
$f_a$	: Non-contact adhesive force at zero overlap.
$\delta_a$	: Non-contact separation between particles at which attractive force becomes active.
$k_c^a$	: Strength of non-contact adhesive force.

# 1 Introduction

Flows of granular materials are ubiquitous in industry and nature. For this reason, the past decade has witnessed a strong interest in better understanding of their behavior. Especially, the impact of fine particles with particles/surfaces is a fundamental problem. The interaction force between two particles is a combination of elasto-plastic deformation, viscous dissipation, and adhesion – due to both contact and long-range non-contact forces. Pair interactions that can be used in bulk simulations with many contacts per particle are the focus, and we use the singular special case of pair interaction to understand them.

Different regimes are observed for two colliding particles: For example a particle can either stick to another particle/surface or it rebounds, depending upon the relative strength of adhesion and impact velocity, size and material parameters. This problem needs to be studied in detail, as it forms the base for understanding more complex, many-particle flows in realistic systems, related to e.g. astrophysics (dust agglomeration, Saturn’s rings, planet formation) or industrial processes (handling of fine powders, granulation, filling and discharging of silos). Particularly interesting is the interaction mechanism for adhesive materials such as asphalt, ice particles or clusters/agglomerates of fine powders (often made of even smaller primary particles). Some materials can be physically visualized as having a plastic outer shell with a rather stiff, elastic inner core. Moreover, the analysis can be applied to particle-surface collisions in kinetic spraying, in which the solid micro-sized powder is accelerated towards a substrate. In cold spray, bonding occurs when impact velocities of particles exceed a critical value, that depends on various material parameters [43, 60, 71] but for even larger velocities particles rebound [70, 74]. Due to the inhomogeneity of most realistic materials, their non-sphericity, and their surface irregularity, the goal is not to include all the possible details – but rather to catch the essential phenomena and ingredients, finding a compromise between simplicity and realistic contact mechanics.

## 1.1 Contact Models Review

Computer simulations have turned out to be a powerful tool to investigate the physics of particulate systems, especially valuable as there is no generally accepted theory of granular flows so far, and experimental difficulties are considerable. A very popular simulation scheme is an adaptation of the classical Molecular Dynamics technique called Discrete Element Method (DEM) (for details see Refs. [2, 7, 15, 25, 28, 29, 49, 54, 61]). It consists of integrating Newton’s equations of motion for a system of “soft”, deformable grains, starting from a given initial configuration. DEM can be successfully applied to adhesive particles, if a proper force-overlap model (contact model) is given.

Brilliantov et al. [4] investigated the collision of adhesive viscoelastic spheres and presented a general analytical expression for their collision dynamics, but we rather turn to plastic contact deformations in the following. The JKR model [21] is a widely accepted adhesion model for elastic spheres and gives an expression for the normal force. Later, Derjaguin et al. [11] considered that the attractive forces act only just outside the contact zone, where surface separation is small. One interesting model for dry adhesive particles was proposed by Molerus [35, 36], which explained consolidation and non-rapid flow of adhesive particles in terms of adhesion forces at particle contacts. Thornton and Yin [53] compared the results of elastic spheres with and without adhesion and Thornton, later on in Ref. [52], extended this work to adhesive elasto-plastic spheres. Molerus’s model was further developed by Tomas, who introduced a contact model [55–57] that couples elasto-plastic contact behavior with non-linear adhesion and hysteresis, which involves dissipation and a history (compression) dependent adhesive force. The contact model subsequently proposed by Luding [29, 33, 34] works in the same spirit as the one of Tomas [56], only reducing complexity by using piecewise linear branches in an otherwise still highly non-linear contact model. In [29], the short ranged non-contact force beyond contact was not specified as in the present study. Complex details like a possible non-linear Hertzian law for small deformation,

and non-linear load-unload hysteresis are over-simplified in the model as compared to Tomas [56]. This is partly due to the lack of experimental reference data or theories, but also to keep the model as simple as possible. The model contains the basic mechanisms, elasticity, plasticity and adhesion as relevant for fine, dry powders and shell-core materials. A possible connection between the microscopic contact model and the macroscopic, continuum description for adhesive particles was recently proposed by Luding and Alonso-Marroquin [30]. Walton et al. [64,69] proposed a contact model which works in the same spirit as that of Luding [29] and Tomas [56], but separates the rate of pull-off force from the slope of tensile attractive force. Jiang et al. [18] experimentally investigated the force-displacement behavior of idealized bonded granules, which was later implemented in DEM in [19] to study the mechanical behavior of loose cemented granular material. Kempton et al. [22] proposed a meso-scale contact model combining linear hysteretic, simplified JKR and linear bonding force models, to simulate agglomerates of sub-particles. Recently a contact model is proposed by Thakur et al. [47], which works in the same spirit as Luding's model, but treats loading and un/re-loading behaviors non-linearly. The authors used the model to study the scaling of DEM parameters in an uniaxial test simulation in [46].

When two particles collide, the behavior is intermediate between the extremes of perfectly elastic and fully inelastic, possibly fragmenting collisions. The elasticity of the collision can be best described by the coefficient of restitution, which is the ratio of magnitude of post-collision and pre-collision normal relative velocities of the particles. It quantifies the amount of energy not dissipated during the collision. For the case of plastic and viscoelastic collisions, it was suggested that dissipation should be dependent on impact velocity [?, 20, 24, 67], as can be realized by viscoelastic forces [6, 24, 27, 31] and follows from plastic deformations too [73]. An early experimental study on micrometer adhesive polystyrene latex spheres was done by Dahneke [9, 10]. He observed sticking of adhesive particles for low velocities, and an

increasing coefficient of restitution for velocity higher than a critical threshold. Wall et al. [63], confirmed these findings for highly mono-disperse ammonium particles. Thornton et al. [52] and Brilliantov et al. [4] presented adhesive visco-elasto-plastic contact models in agreement with these experiments. Work by Sorace et al. [44] further confirms the sticking at low velocities for particle sizes of the order of a few  $\mu\text{m}$ . Li et al. [26] proposed a dynamical model based on JKR for the impact of micro-sized spheres with a flat surface. Jasevičius et al. [16, 17] have recently presented the rebound behavior of ultrafine silica particles using the contact model from Refs. [55–58]. Rozenblat et al. [?] have recently proposed an empirical relation between impact velocity and compression force.

## 1.2 Model classification

Since our focus is on dry particles, we do not review the diverse work involving liquid [14] or strong solid bridges [3] here. Even though oblique collisions between two particles are of practical relevance and have been studied in detail by Thornton et al. [50, 51], here we focus on central normal collisions without loss of generality. Finally, we also disregard many details of non-contact forces, as e.g. due to van der Waals forces, for the sake of brevity, but will propose a simple mesoscale non-contact force model in section 2.3.

Based on our review of adhesive, elasto-visco-plastic contact models, we propose here a (partial) classification, by dividing them into three groups: (1) Academic, (2) Mesoscopic, and (3) Realistic, detailed contact models. Here we review adhesive elastic, and elasto-plastic contact models only. A detailed review concerning the effects of various forces on adhesion of fine particles is nicely reviewed in [65].

1. **Academic contact models** allow for easy analytical solution, as for example the linear spring-dashpot model [27], or piece-wise linear models with constant unloading stiffness (see e.g. Walton and Braun [68] (constant coefficient of resti-



tution mode)), which feature a constant coefficient of restitution, independent of impact velocity. Also the Hertzian visco-elastic models, belong to this class, even though they provide a velocity dependent coefficient of restitution, for a summary see [27]. However, no academic model describes particle deformation that would be practically relevant, as their range of strict validity is extremely limited.

2. **Mesoscopic contact models** are a compromise, (i) still rather easy to implement, (ii) aimed for fast ensemble/bulk-simulations with many particles and various materials, but (iii) not matching all the minute contact details of every single contact, they are often piece-wise linear, e.g., with a variable unloading stiffness or with an extended adhesive force (Walton and Braun [68] (variable coefficient of restitution mode), Luding [29], Walton [69], Thakur et al. [38, 47, 48]), Pasha et al. [?].
3. **Realistic, full-detail contact models** have (i) the most realistic, but often rather complicated formulation, (ii) can reproduce with similar precision the pair interaction and the bulk behavior, but (iii) are valid only for the limited class of materials they are particularly designed for, since they do include all the minute details of these interactions. As a few examples, there are:

- (a) **visco-elastic models:** Walton [66], Brilliantov [4, 5], Haiat [12];
- (b) **adhesive elastic models:** JKR [21], Dahneke [8], DMT [11], Thornton and Yin [53];
- (c) **adhesive elasto-plastic models:** Molerus [35], Thornton and Ning [52], Tomas [55–58].

Since our main goal is to define and apply contact models to simulate the bulk behavior of assemblies of many fine particles (for which no valid realistic model is available), we focus on the second class, mesoscopic models.

### 1.3 Focus and Overview of this study

In particular, we study the dependence of the coefficient of restitution for two meso-particles on impact velocity and contact/material parameters, for a wide range of impact velocities, using a generalized version of the contact model by Luding [29], extended by a non-contact force term. We observe sticking of particles at low velocity, which is consistent with previous theoretical and experimental works [44, 52, 63]. Pasha et al. [?] recently also reproduced the low velocity sticking using an extension of a similar, simpler model [33]. Above a certain small velocity, dissipation is not strong enough to dissipate all relative kinetic energy and the coefficient of restitution increases. We want to understand the full regime of relative velocities, and thus focus also on the less explored intermediate and high velocity regimes, as easily accessible in numerical simulations. In the intermediate regime, we observe a decrease of the coefficient of restitution, as observed previously for idealized particles, see e.g. Refs. [4, 52], but with different functional behavior as predicted by some realistic models, a property that can be tuned by simple modifications to the mesoscopic model. Tanaka et al. [45] have recently reported similar results, when simulating the collision of more realistic dust aggregates, made by many thousands of nanoparticles that interact via the JKR model. With further increase in impact velocity, we find a second interesting sticking regime due to the increasing adhesive dissipation with respect to plastic dissipation. Finally, since the physical systems under consideration also are viscous in nature, we conclude with some simulations with added viscous damping.

An exemplary application of our model that leads to the unexpected high velocity sticking and rebound regimes is, among others, the study of coating processes in cold sprays, where researchers are interested in the effect of the impact velocity on the deposition efficiency of the powder on a substrate. In this process, bonding/coating happens when the impact velocity of the particles exceeds a critical velocity, with values in the order  $10^2$  m/s. Interestingly, when the velocity is further increased the particles do not

bond to the substrate anymore, with a decrease of the deposition efficiency (inverse of coefficient of restitution) [70]. Schmidt et al. [43] have used numerical simulations to explore the effect of various material properties on the critical velocity, while Zhou et al. [74] studied the effect of impact velocity and material properties on the coating process. The data show that properties of both particle and substrate influence the rebound, the details of which go beyond the scope of this study. Using our model we can explore the dependence of the deposition efficiency on the impact velocity, helping the interaction between different communities.

In section 2, we introduce the DEM simulation method and the basic normal contact models, which are further elaborated on in the following section 3, where the coefficient of restitution is computed. Dimensionless contact parameters are proposed in section 4.1, the dependence on contact adhesion is described in section 4.2, the effect of viscosity in section 4.3, and some asymptotic solutions are given in section 4.4. The study is concluded in section 5.

## 2 Discrete Element Method

The elementary units of granular materials are mesoscopic grains, which deform under stress. Since the realistic and detailed modeling of real particles in contact is too complicated, it is necessary to relate the interaction force to the overlap  $\delta$  between two particles. Note that the evaluation of the inter-particle forces based on the overlap may not be sufficient to account for the inhomogeneous stress distribution inside the particles and possible multi-contact effects [20]. This price has to be paid in order to simulate larger samples of particles with a minimal complexity and still taking various physical contact properties like non-linear contact elasticity, plastic deformation or load-dependent adhesion into account.

## 2.1 Equations of Motion

If all forces acting on a spherical particle  $p$ , either from other particles, from boundaries or externally, are known – let their vector sum be  $f_p$  – then the problem is reduced to the integration of Newton’s equations of motion for the translational degrees of freedom (the rotational degrees are not considered here since we focus on normal forces) for each particle:

$$m_p \frac{d^2}{dt^2} r_p = f_p + m_p g \quad (1)$$

where,  $m_p$  is the mass of particle  $p$ ,  $r_p$  its position,  $f_p = \sum_c f_p^c$  is the total force due to all contacts  $c$ , and  $g$  is the acceleration due to volume forces like gravity.

With tools from numerical integration, solving the equations of motion, as nicely described in textbooks as [1, 41, 42], is a straightforward exercise. The typically short-ranged interactions in granular media allow for further optimization by using linked-cell (LC) or alternative methods in order to make the neighborhood search more efficient. However, this is not of concern in this study, since only normal pair collisions are considered.

## 2.2 Normal Contact Force Laws

Two spherical particles  $i$  and  $j$ , with radii  $a_i$  and  $a_j$ ,  $r_i$  and  $r_j$  being the position vectors respectively, interact if they are in contact so that their overlap,

$$\delta = (a_i + a_j) - (r_i - r_j) \cdot n \quad (2)$$

is positive,  $\delta > 0$ , with the unit vector  $n = n_{ij} = (r_i - r_j)/|r_i - r_j|$  pointing from  $j$  to  $i$ . The force on particle  $i$ , from particle  $j$ , at contact  $c$ , can be decomposed into a normal and a tangential part as  $f_i^c := f_i^c = f^n n + f^t t$ , where  $n \cdot t = 0$ ,  $n$  and  $t$  being normal and tangential parts respectively. In this paper, we focus on frictionless particles, that is only normal forces will be considered, for tangential forces and torques, see e.g.

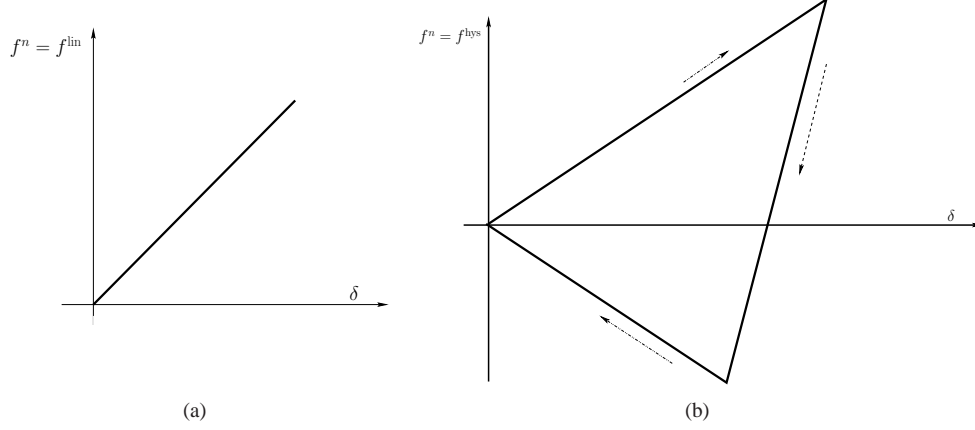


Figure 1: Schematic plots of (a) the linear normal contact model for a perfectly elastic collision, and (b) the force-overlap relation for an elasto-plastic adhesive collision

Ref. [29] and references therein.

In the following, we discuss various normal contact force models, as shown schematically in Fig. 1. We start with the linear contact model (Fig. 1(a)) for non-adhesive particles, before we introduce a more complex contact model that is able to describe the realistic interaction between adhesive, inhomogeneous, slightly non-spherical particles (Fig. 1(b)).

### 2.2.1 Linear Normal Contact Model

Modelling a force that leads to an inelastic collision requires at least two ingredients: repulsion and some sort of dissipation. The simplest normal force law with the desired properties is the damped harmonic oscillator

$$f^n = k\delta + \gamma_0 v^n, \quad (3)$$

with spring stiffness  $k$ , viscous damping  $\gamma_0$ , and normal relative velocity  $v^n = -\vec{v}_{ij} \cdot \vec{n} = -(\vec{v}_i - \vec{v}_j) \cdot \vec{n} = \dot{\delta}$ . This model (also called linear spring dashpot (LSD) model) has the advantage that its analytical solution (with initial conditions  $\delta(0) = 0$  and  $\dot{\delta}(0) = v_0^n$ )

allows the calculations of important quantities very easily [27]. For the non-viscous case, the linear normal contact model is given schematically in Fig. 1(a).

The typical response time (contact duration) and the eigenfrequency of the contact are related as

$$t_c = \frac{\pi}{\omega} \quad \text{and} \quad \omega = \sqrt{(k/m_r) - \eta_0^2} \quad (4)$$

with the rescaled damping coefficient  $\eta_0 = \gamma_0/(2m_r)$ , and the reduced mass  $m_r = m_i m_j / (m_i + m_j)$ . From the solution of the equation of a half-period of the oscillation, one also obtains the coefficient of restitution

$$e_n^{\text{LSD}} = v_f/v_i = \exp(-\pi\eta_0/\omega) = \exp(-\eta_0 t_c) , \quad (5)$$

which quantifies the ratio of normal relative velocities after ( $v_f$ ) and before ( $v_i$ ) the collision. Note that in this model  $e_n$  is independent of  $v_i$ . For a more detailed review on this and other, more realistic, non-linear contact models, see [27, 29] and references therein.

The contact duration in Eq. (4) is also of practical and technical importance, since the integration of the equations of motion is stable only if the integration time-step  $\Delta t$  is much smaller than  $t_c$ . Note that  $t_c$  depends on the magnitude of dissipation: In the extreme case of an over-damped spring (high dissipation),  $t_c$  can become very large (which renders the contact behavior artificial [31]). Therefore, the use of neither too weak nor too strong viscous dissipation is recommended.

### 2.2.2 Adhesive Elasto-Plastic Contacts

Here we apply a variation to previously proposed piece-wise linear hysteretic model [27–29, 55, 68] as an alternative to non-linear spring-dashpot models or more complex hysteretic models [52, 55–57, 62, 72]. It reflects permanent plastic deformation, which might take place at the contact, and stronger attractive (adhesive) forces, both depend-

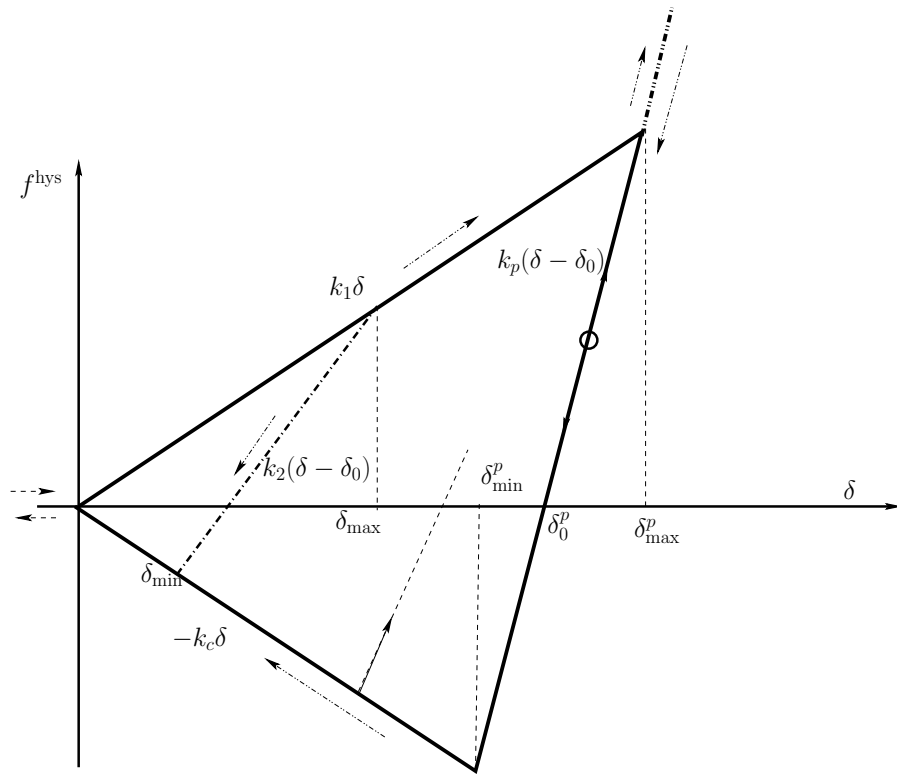


Figure 2: Schematic graph of the piece-wise linear, hysteretic, and adhesive force-displacement model in normal direction.

ing non-linearly on the maximal compression force.

In Fig. 2, the normal force at contact is plotted against the overlap  $\delta$  between two particles. The force law can be written as

$$f^{\text{phys}} = \begin{cases} k_1 \delta & \text{if } k_2(\delta - \delta_0) \geq k_1 \delta \\ k_2(\delta - \delta_0) & \text{if } k_1 \delta > k_2(\delta - \delta_0) > -k_c \delta \\ -k_c \delta & \text{if } -k_c \delta \geq k_2(\delta - \delta_0) \end{cases} \quad (6)$$

with  $k_1 \leq k_2 \leq k_p$ , respectively the initial loading stiffness, the un-/re-loading stiffness and the elastic limit stiffness. The latter defines the limit force branch  $k_p(\delta - \delta_0^p)$ , as will be motivated below in more detail, and  $k_2$  is interpolating between  $k_1$  and  $k_p$ , see Eq. (10). For  $k_c = 0$ , the above contact model reduces to that proposed by Walton and Braun [68], which leads to a variable coefficient of restitution

$$e_n^{\text{WB}} = \sqrt{k_1/k_2}, \quad (7)$$

as proposed by Walton and Braun [68].

During the initial loading the force increases linearly with overlap  $\delta$  along  $k_1$ , until the maximum overlap  $\delta_{\text{max}} = v_i \sqrt{m_r/k_1}$  (for binary collisions) is reached, which is a history parameter for each contact. During unloading the force decreases along  $k_2$ , see Eq. (10), from its maximum value  $k_1 \delta_{\text{max}}$  at  $\delta_{\text{max}}$  down to zero at overlap

$$\delta_0 = (1 - k_1/k_2) \delta_{\text{max}}, \quad (8)$$

where  $\delta_0$  resembles the *permanent plastic contact deformation*. Reloading at any instant leads to an increase of the force along the (elastic) branch with slope  $k_2$ , until the maximum overlap  $\delta_{\text{max}}$  (which was stored in memory) is reached; for still increasing overlap  $\delta$ , the force again increases with slope  $k_1$  and the history parameter  $\delta_{\text{max}}$  has to be updated.



Unloading below  $\delta_0$  leads to a negative, *attractive* (adhesive) force, which follows the line with slope  $k_2$ , until the extreme adhesive force  $-k_c\delta_{\min}$  is reached. The corresponding overlap is

$$\delta_{\min} = \frac{(k_2 - k_1)}{(k_2 + k_c)} \delta_{\max} . \quad (9)$$

Further unloading follows the irreversible tensile branch, with slope  $-k_c$ , and the attractive force  $f^{\text{hys}} = -k_c\delta$ .

The lines with slope  $k_1$  and  $-k_c$  define the range of possible force values and departure from these lines takes place in the case of unloading and re-loading, respectively. Between these two extremes, unloading and re-loading follow the line with slope  $k_2$ . A non-linear un-/re-loading behavior would be more realistic, however, due to a lack of detailed experimental informations, the piece-wise linear model is used as a compromise; also it is easier to implement. The elastic  $k_2$  branch becomes non-linear and ellipsoidal, when a moderate normal viscous damping force is active at the contact, as in the LSD model.

In order to account for realistic load-dependent contact behavior, the  $k_2$  value is chosen dependent on the maximum overlap  $\delta_{\max}$ , i.e. *particles are more stiff for larger previous deformation* and the dissipation is dependent on deformation. The dependence of  $k_2$  on overlap  $\delta_{\max}$  is chosen empirically as linear interpolation (in the same spirit as Walton and Braun [68]):

$$k_2(\delta_{\max}) = \begin{cases} k_p & \text{if } \delta_{\max}/\delta_{\max}^p \geq 1 \\ k_1 + (k_p - k_1)\delta_{\max}/\delta_{\max}^p & \text{if } \delta_{\max}/\delta_{\max}^p < 1 \end{cases} \quad (10)$$

where  $k_p$  is the (maximal) elastic stiffness, and

$$\delta_{\max}^p = \frac{k_p}{k_p - k_1} \phi_f \frac{2a_1a_2}{a_1 + a_2} , \quad (11)$$

is the plastic flow limit overlap, with  $\phi_f$  the dimensionless plasticity depth,  $a_1$  and  $a_2$  being the radii of the two particles. This can be further simplified to

$$\delta_0^p = \phi_f a_{12}, \quad (12)$$

where  $\delta_0^p$  represents the plastic contact deformation at the limit overlap, and  $a_{12} = \frac{2a_1 a_2}{a_1 + a_2}$  is the reduced radius. In the range  $\delta_{\max} < \delta_{\max}^p$ , the dependence of  $k_2$  can also be written as follows:

$$k_2 = k_1 + \frac{(k_p - k_1)}{k_1 \delta_{\max}^p} f^{\max}, \quad (13)$$

where  $f^{\max} = k_1 \delta_{\max}$ , which is same as equation 4 in [68] with  $S = \frac{(k_p - k_1)}{k_1 \delta_{\max}^p}$ .

From energy balance, one can define the “plastic” limit velocity

$$v_p = \sqrt{k_1 / m_r} \delta_{\max}^p, \quad (14)$$

below which the contact behavior is elasto-plastic, and above which the perfectly elastic limit-branch is reached. Impact velocities larger than  $v_p$  can have consequences, as discussed next.

In summary, the adhesive, elasto-plastic, hysteretic normal contact model is defined by the four parameters  $k_1$ ,  $k_p$ ,  $k_c$  and  $\phi_f$  that, respectively, account for the initial plastic loading stiffness, the maximal, plastic limit (elastic) stiffness, the adhesion strength, and the plastic overlap-range of the model; it also involves an empirical choice for the non-linear, load-dependent, intermediate elastic branch stiffness  $k_2$ .

### 2.2.3 Motivation of the original contact model

To study a collision between two ideal, homogeneous spheres, one should refer to realistic, full-detail contact models with a solid experimental and theoretical foundation [21, 52, 55]. These contact models feature a small elastic regime and the particles

increasingly deform plastically with increasing, not too large deformation (overlap). During unloading, their contacts end at finite overlap due to flattening. Otherwise, besides many smaller model details there exist various such models. However, one has to consider also the non-contact forces that are often neglected for very large particles, but become dominant and hysteretic as well as long-ranged for rather small spheres [55]. A mesoscopic model that compromises on the details of the contact model, but follows the flat contact detachment philosophy was recently proposed in Ref. [?].

The mesoscopic contact model used here was originally proposed by Luding [29] and follows a different approach in two respects: (i) it introduces a limit to the plastic deformation of the particles/material for various reasons as summarized below in subsection 2.2.4, and (ii) the contacts are not idealized as perfectly flat, and thus do not have to lose mechanical contact immediately at un-loading, as will be detailed in the subsection 2.2.5.

Note that a limit to the slope  $k_p$  that resembles *a different contact behavior at large deformations* has various physical and numerical reasons:

- (0) due to the wide probability distribution of forces in bulk granular matter, only few contacts should reach the limit, which should not effect much the collective behavior;
- (i) in many particle systems, for large deformations the particles cannot be assumed to be spherical anymore, as they deform plastically or even could break;
- (ii) from the macroscopic point of view, too large deformations would lead to volume fractions larger than unity, which for most materials (except highly micro-porous, fractal ones) would be unaccountable;
- (iii) at small deformation, contacts are due to surface roughness realized by multiple surface asperities and at large deformation, the single pair point-contact argument breaks down and multiple contacts of a single particle can not be assumed to be independent anymore;
- (iv) numerically in a bulk simulation the time step is chosen such that it is well below

the minimal contact duration of all the contacts. If  $k_2$  is not limited this minimum could become very small so that the required time step would have to be reduced below practical values, only because of some extreme contacts.

Following two subsections discuss the two major differences of the present piece-wise linear model as compared to other existing models: (i) the elastic limit branch, and (ii) the elastic re-loading or non-contact-loss, as well as their reasons, relevance and possible changes/tuning – in cases needed.

#### **2.2.4 Shortcomings, physical relevance and possible tuning**

In the context of collisions between perfect homogeneous elasto-plastic spheres, a purely elastic threshold/limit and enduring elastic behavior after a sharply defined contact-loss are indeed questionable, as the plastic deformation of the single particle cannot become reversible/elastic. Nevertheless, there are many materials that support the idea of a more elastic behavior at very high impact velocity (or contact force).

In the following, we will list some of these cases and extensively comment on them.

**Mesoscopic contact model applied to real materials:** First we want to recall that the present model is mainly aimed to reproduce the behavior of multi-particle systems of realistic fine and ultra-fine powders, which are typically non-spherical and often mesoscopic in size with internal micro-structure and micro-porosity on the scale of typical contact deformation. For example, think of clusters/agglomerates of primary nano-particles that form fine micron-sized secondary powder particles, or other fluffy materials. The primary particles are possibly better described by other contact models, but in order to simulate a reasonable number of secondary particles one cannot rely on this bottom-up approach and better uses a meso-contact model. During the bulk compression of such a system, the material deforms plastically and its internal porosity reduces. Plastic deformation diminishes if the primary particles are elastic/stiff and the material has become dense, almost non-porous. Beyond this point the system deform

more elastically, i.e. the stiffness becomes high and the (irrecoverable) deformations are much smaller than initially.

In their compression experiments of granular beds with micrometer sized granules of micro-crystalline cellulose, Persson et al. [40] found that a contact model where a limit on plastic deformation is introduced can very well describe the bulk behavior. Experimentally they observe a strong elasto-plastic bulk-behavior for the assembly at low compression strain/stress. In this phase the height of the bed decreases, irreversibly and almost linearly with the applied load, while the deviation from linearity strongly increases beyond a certain strain/stress, with a dramatic increase of the stiffness of the aggregate. They associate the change in the behavior to the loss of porosity and the subsequent more elastic bulk response to the particles that are now closely in touch with each other. In this new, considerably denser configurations, not much more void reduction is allowed and thus the behavior gets more elastic. While the elastic limit in the contact model does not affect the description of the bulk behavior in the first part, the threshold is found to play a key role in order to reproduce the material stiffening (see Fig. 8 in Ref. [40]).

Note that in an assembly of particles, not all the contacts will reach the limit branch and deform elastically simultaneously. That is, even if few contacts are in the elastic limit, the system will always retain some plasticity, hence *the assembly will never be fully elastic*.

**Application to pair interactions:** Interestingly, the contact model in Sec. 2.2.2 is suitable to describe the collision between pairs of particles, when special classes of materials are considered, such that the behavior at high velocity and thus large deformation drastically changes.

(i) *Core-shell materials*. The model is perfectly suited for plastic core-shell materials, such as asphalt or ice particles, having a “soft” plastic outer shell and a rather stiff, elastic inner core. For such materials the stiffness increases with the load due to an

increasing contact surface. For higher deformations, contact between the inner cores can take place, which turns out to be almost elastic when compared to the behavior of the external shell. The model was successfully applied to model asphalt, where the elastic inner core is surrounded by a plastic oil or bitumen layer [39]. Alternatively, the plastic shell can be seen as the range of overlaps, where the surface roughness and inhomogeneities lead to a different contact mechanics as for the more homogeneous inner core.

(ii) *Cold spray*. An other interesting system that can be effectively reproduced by introducing an elastic limit in the contact model is cold spray. Researchers have experimentally and numerically shown that spray-particles rebound from the substrate at low velocity, while they stick at intermediate impact energy [37, 43, 60, 71]. Wu et al. [70] experimentally found that rebound re-appears with a further increase in velocity (Fig. 3 in Ref. [70]). Schmidt et al. [43] relate the decrease of the deposition efficiency (inverse of coefficient of restitution) to a transition from a plastic impact to hydrodynamic penetration (Fig. 16 in Ref. [43]). Recently Moridi et al. [37] numerically studied the sticking and rebound processes, by using the adhesive elasto-plastic contact model of Luding [29], and their prediction of the velocity dependent behavior is in good agreement with experiments.

(iii) *Sintering*. As an additional example, we want to recall that the present meso-contact model has already been applied to the case of sintering, see Ref. [34]. For large deformations, large stresses, or high temperatures, the material goes to a fluid-like state rather than being solid. Hence, the elasticity of the system (nearly incompressible melt) determines its limit stiffness, while  $\phi_f$  determines the maximal volume fraction that can be reached.

All the realistic situations described above clearly hint at a modification in the contact phenomenology that can not be described anymore by an elasto-plastic model beyond some threshold in the overlap/force. The limit stiffness  $k_p$  and the plastic layer

depth  $\phi_f$  in our model allow the transition of the material to a new state. Dissipation on the limit branch – which otherwise would be perfectly elastic – can be taken care of, by a viscous damping force (as the simplest option). Due to viscous damping, the unloading and re-loading will follow different paths, so that the collision will never be perfectly elastic, which is in agreement with the description in Jasevičius et al. [16, 17] and will be shown below in subsection 4.3.

Finally, note that an elastic limit branch is surely not the ultimate solution, but a simple first model attempt – possibly requiring material- and problem-adapted improvements in the future.

**Tuning of the contact model:** The change in behavior at large contact deformations is thus a feature of the contact model which allows us to describe many special types of materials. Nevertheless, if desired, without changing the model, the parameters can be tuned in order to reproduce the behavior of materials where the plasticity keeps on increasing with deformation. The limit-branch where plastic deformation ends is defined by the dimensionless parameters plasticity depth,  $\phi_f$ , and (maximal) elastic stiffness,  $k_p$ . Owing to the flexibility of the model, it can be tuned such that the limit overlap is set to a much higher value which is never reached by the contacts. When the new value of  $\phi_f'$  is chosen, a new  $k_p'$  can be calculated to describe the behavior at higher overlap (as detailed in Appendix B). In this way the model with the extended  $\phi_f'$  exhibits elasto-plastic behavior for a higher velocity/compression-force range, while keeping the physics of the system for smaller overlap identical to the one with small  $\phi_f$ .

### 2.2.5 Irreversibility of the tensile branch

Finally we discuss a feature of the contact model in [29], that postulates the irreversibility, i.e. partial elasticity, of the tensile  $k_c$  branch, as discussed in Sec. 2.2.2. While this is unphysical in some situations, e.g. for homogeneous plastic spheres, we once again

emphasize that we are interested in non-homogeneous, non-spherical meso-particles, as e.g. clusters/agglomerates of primary particles in contact with internal structures of the order of typical contact deformation.

Only for ideal, perfect, elasto-plastic adhesive spheres that experience a large enough tensile force, the particles detach with a (perfect) flattened surface due to plasticity. In almost all other cases, the shape of the detaching surfaces and the subsequent behavior depend on the relative strength of plastic, attractive, and other contact mechanisms. Moreover, other details like particle rotation can also play a role. Few examples include core-shell materials [39], assemblies of micro-porous fine powders [40] or atomic nanoparticles [45]. We first briefly discuss the case of ideal elasto-plastic adhesive particles and later describe the behavior of many particle systems, which is the main focus of this work.

For ideal homogeneous particles with radius of the order of millimeters [?, 52], a permanently flattened surface is created during deformation of the order of micrometers and the plastic dissipation during mechanical contact is dominant with respect to the van der Waals force. When the particles detach during unloading, the force suddenly drops to zero from the tensile branch. During non-contact, further un- and re-loading involves no force; when the contact is re-established it also is assumed to be mostly elastic, following the previous contact-unloading path. Thus re-established contacts have little or no plastic deformation until the (previously reached) maximum overlap is reached again – from when on strong plasticity kicks in again.

On the other hand for ultra-fine ideal spherical particles of order of macro-meters [55, 58, 59], the van der Waals force is much stronger and unloading adhesion is due to purely non-contact forces. Therefore, the non-contact forces do not vanish and even extend beyond the mechanical first contact distance. The contact model of Tomas [55, 58] is reversible for non-contact and features a strong plastic deformation for the re-established contact – in contrast to the previous case of large particles.



The contact model by Luding [29] follows similar considerations as others, except for the fact that the mechanical contact does *not* detach, as discussed next. The irreversible, elastic re-loading before complete detachment can be seen as a compromise between small and large particle mechanics, i.e. between weak and strong attractive forces. It also could be interpreted as a premature re-establishment of mechanical contact, e.g., due to a rotation of the particles. Detachment and remaining non-contact is only then valid if the particles do not rotate relative to each other; in case of rotations, both sliding and rolling degrees of freedom can lead to a mechanical contact much earlier than in the ideal case of a perfect normal collision of ideal particles. In the spirit of a mesoscopic model, the irreversible contact model is due to the ensemble of possible contacts, where some behave like imagined in the ideal case, whereas some behave strongly different, e.g., due to some relative rotation. However, there are several other good reasons to consider an irreversible unloading branch.

In the case of asphalt (core-shell material with a stone core and bitumen-shell), dependent on the composition of the bitumen, it can contain a considerable amount of fine solids that will behave softly for loading, but rather stiff for re-loading (elastic  $k_2$  branch). (Bitumen with fine fillers is referred to as “mastic”, but a more detailed study of this class of materials goes beyond the scope of this study.) [39]

For atomistic nano-particles and for porous particles, one thing in common is the fact the typical deformations can be much larger than the primary particles inhomogeneities and that the adhesion of the primary particles is very strong, which leads to their re-arrangements (see Fig. 5 in Ref. [45]). That is the bulk material will deform plastically (irreversibly) even if the primary particles can be assumed to be perfectly elastic. We can not assume permanent ideal flattening and full loss of mechanical contact during unloading for the mesoscopic particles: Many contacts between the primary particles and surface inhomogeneities will be lost, but – due to their strong attraction – many others will keep their contacts. Strong clusters of primary particles will remain

intact and can form bridges (threads) or clumps during unloading – which either keep the two surfaces in contact beyond the idealized detachment point or can lead to an elastic repulsion due to a clump-particle sitting between the surfaces (see Fig. 3 in Ref. [29]).

When re-loading, the (elastic) connecting elements influence the response; rearrangements of the primary particles (and clusters) happen on the surface, leading to its reshaping – leaving a surely non-flat contact surface.

Also in this case, as often mentioned for granular systems, the interaction of several elastic particles does not imply bulk elasticity of the assembly, due to rearrangements. Thus, in the present model an irreversible tensile branch is assumed, without distinction between the behavior before and after the first contact-loss-point other than the intrinsic non-linearity in the model: The elastic stiffness for re-loading  $k_2$  decreases the closer it comes to  $\delta = 0$ ; in the present version of the contact model,  $k_2$  for unloading from the  $k_1$  branch and for re-loading from the  $k_c$  branch are exactly matched.

As a final remark, for almost all models on the market – due to convenience and numerical simplicity, in case of complete detachment  $\delta < 0$  – the contact is set to its initial state, since it is very unlikely that the two particles will touch again at exactly the same contact point as before. On the other hand in the present model a long-range interaction is introduced, in the same spirit as [56, 58]. Reloading in the non-contact ( $\delta < 0$ ) regime is perfectly elastic, as it refers to the non-contact of surfaces and is due only to long-range attractive (van der Waals) forces, as will be detailed in the next subsection.

### 2.3 Non-contact normal force

It has been shown in many studies that long-range interactions are present when dry adhesive particles collide, i.e. forces are present even for negative overlap  $\delta$  [29, 52, 58, 59]. In the previous section, we have studied the force laws for contact overlap

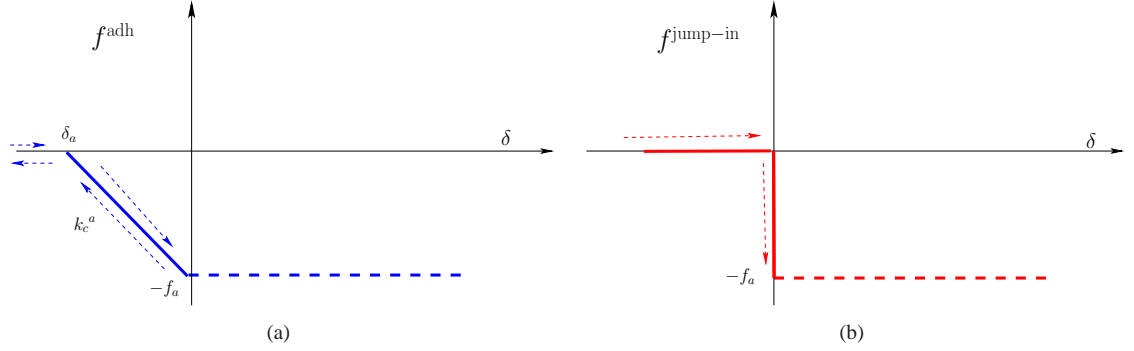


Figure 3: Schematic plots of (a) the non-contact adhesive force-overlap relation and (b) the non-contact jump-in force-overlap relation.

$\delta > 0$ . In this section we introduce a description for non-contact, long range, adhesive forces, focusing on the two non-contact models schematically shown in Fig. 3 – both piece-wise linear in the spirit of the mesoscopic model – namely the reversible model and the jump-in (irreversible) non-contact models (where the latter could be seen as an idealized, mesoscopic representation of a liquid bridge, just for completeness). Later, in the next section, we will combine non-contact and contact forces.

### 2.3.1 Reversible Adhesive force

In Fig. 3(a) we consider the reversible attractive case, where a (linear) van der Waals type long-range adhesive force is assumed. The force law can be written as

$$f^{\text{adh}} = \begin{cases} -f_a & \text{if } \delta > 0 \\ -k_c^a \delta - f_a & \text{if } 0 \geq \delta > \delta_a \\ 0 & \text{if } \delta_a > \delta \end{cases} \quad (15)$$

with the range of interaction  $\delta_a = -f_a/k_c^a$ , where  $k_c^a > 0$  is the adhesive strength of the material and  $f_a > 0$  is the (constant) adhesive force magnitude, active for overlap  $\delta > 0$  in addition to the contact force. When  $\delta = 0$  the force is  $-f_a$ . The adhesive force  $f^{\text{adh}}$  is active when particles are closer than  $\delta_a$ , when it starts increase/decrease linearly

along  $-k_c^a$ , for approach/separation respectively. In the rest of the paper, for the sake of simplicity and without loss of generality, the adhesive strength will be chosen as coincident with the contact adhesive stiffness in Sec. 2.2.2, that is  $k_c^a = k_c$ .

### 2.3.2 Jump-in (Irreversible) Adhesive force

In Fig. 3(b) we report the behavior of the non-contact force versus overlap when the approach between particles is described by a discontinuous (irreversible) attractive law. The jump-in force can be simply written as

$$f^{\text{jump-in}} = \begin{cases} 0 & \text{if } \delta < 0 \\ -f_a & \text{if } \delta \geq 0 \end{cases}. \quad (16)$$

As suggested in previous studies [4, 21, 52], there is no attractive force before the particles come into contact; the adhesive force becomes active and suddenly drops to a negative value,  $-f_a$ , at contact, when  $\delta = 0$ . The jump-in force resembles the limit case  $k_c^a \rightarrow \infty$  of Eq. (15). Note that the behavior is defined here only for approach of the particles. We assume the model to be irreversible, as in the unloading stage, during separation, the particles will not follow this same path (details will be discussed below).

## 3 Coefficient of Restitution

As already mentioned, we can quantify the amount of dissipated energy relative to the incident kinetic energy in terms of the coefficient of restitution  $e$ , by using the expression  $1 - e^2$ .

When we consider a pair collision, with particles approaching from infinite dis-

tance, the coefficient of restitution can be defined as

$$e = \frac{v_f^\infty}{v_i^\infty} \quad (17a)$$

and further decomposed as

$$e = \frac{v_f^\infty}{v_f} \frac{v_f}{v_i} \frac{v_i}{v_i^\infty} = \varepsilon_o e_n \varepsilon_i, \quad (17b)$$

where three different regimes have been introduced to describe the pair interaction.  $\varepsilon_i$  and  $\varepsilon_o$  are the pull-in and pull-off coefficients of restitution, that describe the non-contact parts of the interaction ( $\delta < 0$ ), for approach and separation of particles respectively, while  $e_n$  is the coefficient of restitution defined for particle in contact ( $\delta > 0$ ).  $v_i^\infty$  and  $v_f^\infty$  denote the approach and separation velocities at infinity distance, when the (short- and long-range) interaction force is zero.  $v_i$  is the approaching velocity at zero contact overlap  $\delta = 0$  (start of contact) and  $v_f$  is the separation velocity at zero overlap  $\delta = 0$  when the particles are separating (end of contact).

In the following, we will first analyze each term in Eq. (17b) separately, based on energy considerations. Then we will show combined contact models using the non-contact and contact components described in sections 2.2-2.3 and provide the coefficient of restitution for this wide class of models.

### 3.1 Pull-in coefficient of restitution

In order to describe the pull-in coefficient of restitution  $\varepsilon_i$  we focus on the two non-contact models proposed in Sec. 2.3, as simple interpretations of the adhesive force during the approach of the particles.

When the *reversible adhesive* contact model is used, the energy conservation argument

$$\frac{1}{2} m_r v_i^{\infty 2} = \frac{1}{2} f_a \delta_a + \frac{1}{2} m_r v_i^2 \quad (18a)$$

yields the following expression for  $\epsilon_i$ :

$$\epsilon_i^{\text{adh}} = \frac{v_i}{v_i^\infty} = \sqrt{1 - \frac{f_a \delta_a}{m_r v_i^{\infty 2}}} = \sqrt{1 + \frac{f_a^2 / k_c}{m_r v_i^{\infty 2}}} . \quad (18b)$$

The pull-in coefficient of restitution increases with increasing adhesive force magnitude  $f_a$  due to increase in attractive force and decreases with the adhesive strength of the material  $k_c$ . On the other hand, if the *irreversible adhesive jump-in* model is implemented, a constant value  $\epsilon_i^{\text{jump-in}} = 1$  is obtained, as  $f^{\text{jump-in}} = 0$  for  $\delta < 0$  and the velocity is constant  $v_i = v_i^\infty$ .

### 3.2 Normal coefficient of restitution

When focusing on the contact coefficient of restitution  $e_n$  and writing the energy balance between the start and end of contact interaction, we get

$$\frac{1}{2} m_r v_i^2 = W_{\text{diss}} + \frac{1}{2} m_r v_f^2 \quad (19a)$$

and

$$e_n = \frac{v_f}{v_i} = \sqrt{1 - \frac{2W_{\text{diss}}}{m_r v_i^2}} , \quad (19b)$$

where  $W_{\text{diss}}$  denotes the amount of energy dissipated during the collision.

If the *linear* contact model (see Sec. 2.2.1) is considered in the absence of viscous damping (LS),  $W_{\text{diss}}$  is zero, hence the normal coefficient of restitution  $e_n^{\text{LS}} = 1$ . On the other hand, for either viscous damping or in the case of *adhesive elasto-plastic* contacts (see Sec 2.2.2), there is finite dissipation. As  $W_{\text{diss}}$  is always positive, the normal coefficient of restitution is always smaller than unity, i.e.  $e^{\text{LSD}} < 1$  and  $e_n^{\text{HYS}} < 1$ . The coefficient of restitution for the linear spring dashpot model is given in Eq. (5), while the elasto-plastic contact model will be discussed below.

### 3.3 Pull-off coefficient of restitution

The pull-off coefficient of restitution is defined for particles that lose contact and separate, using the *adhesive reversible* model as described in section 2.3.1.

By assuming energy conservation

$$\frac{1}{2}mv_f^{\infty 2} = \frac{1}{2}f_a\delta_a + \frac{1}{2}mv_f^2, \quad (20a)$$

we obtain the following expression

$$\epsilon_o = \frac{v_f^{\infty}}{v_f} = \sqrt{1 + \frac{f_a\delta_a}{mv_f^2}} = \sqrt{1 - \frac{f_a^2/k_c}{mv_f^2}}. \quad (20b)$$

Similarly to what already seen for Eq. 18b, the pull-off coefficient of restitution depends on both the adhesive force magnitude  $f_a$  and strength  $k_c$ , other than the separation velocity  $v_f$ . As the particles feel an attractive force during unloading, part of their kinetic energy is lost and hence  $\epsilon_o < 1$  in Eq. (20b).

It is worthwhile to notice that the force-overlap picture described above, with  $\epsilon_o$  defined as in Eq. (20b) refers to a system with sufficiently high impact velocity, so that the particles can separate with a finite kinetic energy at the end of collision. That is

$$v_f^2 > f_a^2/(mk_c) =: (v_f^a)^2 \quad (21)$$

or, equivalently,  $v_i^{\infty} > v_f^a/(e_n\epsilon_i)$ , where  $v_f^a$  denotes the maximum relative velocity at which particles actually can separate. On the other hand, if the kinetic energy reaches zero before the separation, e.g. during the unloading path, the particles start re-loading along the adhesive branch until the value  $\delta = 0$  is reached and they follow contact law defined for  $\delta > 0$  again.

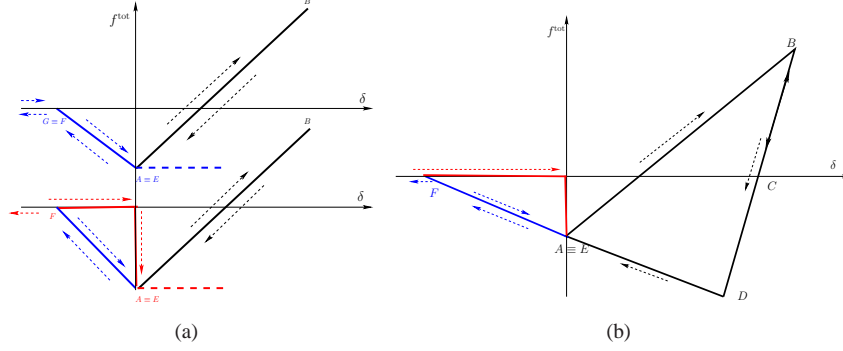


Figure 4: (a) Reversible and irreversible non-contact forces, where the top blue line (for negative overlap) represents the former and the bottom red line (for negative overlap) the latter. The black line for positive overlap represents the linear contact force as superimposed on the non-contact force. (b) Force-displacement law for elasto-plastic, adhesive contacts superimposed on the irreversible non-contact adhesive force.

### 3.4 Combined contact laws

The contact and non-contact models described in previous sections 3.1, 3.2 and 3.3 can be combined in order to obtain the overall description of the system behavior, during approach, contact and final separation of the particles.

For example, the combination of the pull-in, the linear normal and the pull-off components leads to a *reversible adhesive linear* contact model, as shown schematically in the upper part of Fig. 4(a), with coefficient of restitution  $e = \epsilon_o e_n^{\text{LSD}} \epsilon_i^{\text{adh}}$ . On the other hand, by combining the irreversible (jump-in) pull-in, the linear normal and the (reversible) pull-off components (see schematic in the lower part of Fig. 4(a)) we get coefficient of restitution  $e = \epsilon_o e_n^{\text{LSD}} \epsilon_i^{\text{jump-in}}$ .

In the following we will focus on the combination of the irreversible pull-in with the adhesive elasto-plastic and the (reversible) pull-off parts, leading to an *irreversible adhesive elasto-plastic* model, see Fig. 4(b), with  $e = \epsilon_o e_n^{\text{HYS}} \epsilon_i^{\text{jump-in}} = \epsilon_o e_n^{\text{HYS}}$ . For this special case we want to analyze the influence of the adhesive component/parameters on the overall behavior.

In Fig. 5, we plot the coefficient of restitution  $e$  as a function of impact velocity for



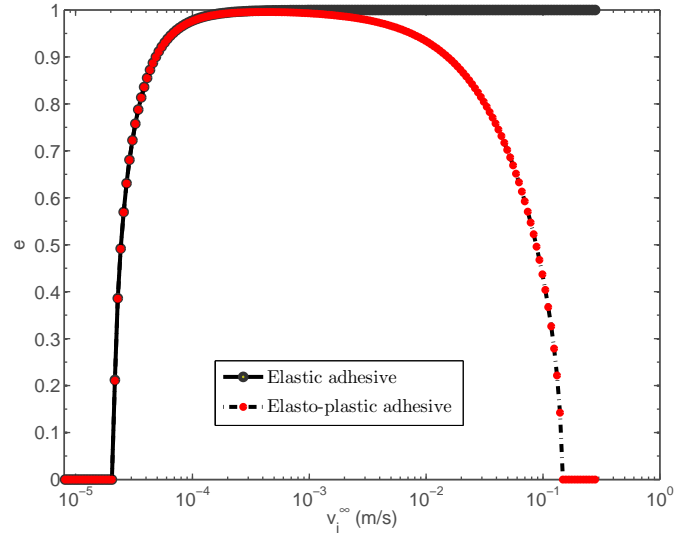


Figure 5: Restitution coefficient  $e$  plotted as a function of the impact velocity  $v_i^\infty e_n \rightarrow e$  and  $v_i \rightarrow v_i^\infty$  for irreversible elastic-adhesive and elasto-plastic adhesive spheres (as given in the inset). Parameters used here are  $k_1 = 10^2 \text{ Nm}^{-1}$ ,  $k_p = 5 \times 10^2 \text{ Nm}^{-1}$ ,  $k_c = 10^2 \text{ Nm}^{-1}$ , and  $f_a = 5 \times 10^{-7} \text{ N}$ , which leads to the low-velocity sticking limit  $v_f^a = 2.1 \times 10^{-5} \text{ m/s}$ , for particles with radius  $1.1 \cdot 10^{-3} \text{ m}$ , density  $2000 \text{ kg/m}^3$ , and mass  $m = 5.6 \times 10^{-6} \text{ kg}$ .

both the irreversible elastic ( $e_n = e_n^{\text{LSD}}$ ) and the irreversible elasto-plastic ( $e_n = e_n^{\text{HYS}}$ ) contact models. We observe that for low velocity the system behaves in a similar fashion in both cases, showing an initial sticking regime, in agreement with previous experimental and numerical results [44, 52, 63]. At higher velocities, a significant difference appears: for elastic adhesive spheres,  $e$  keeps increasing and approaches unity while, for elasto-plastic adhesive spheres,  $e$  starts decreasing at intermediate velocity until it becomes zero at higher velocity. This difference is related with the sources of dissipation in the two models. In the irreversible elastic case, energy is dissipated only due to the pull-off of the particles, which is significant in low velocity range only. On the contrary, for irreversible elasto-plastic spheres, dissipation takes place during both, pull-off and normal contact, stages. The latter, new, effect is negligible for low velocity (hence the two models coincide) but it becomes important for large impact velocity, leading to a second, high velocity, sticking regime, (that will be discussed in detail below).

Furthermore, in Fig. 6, we focus on the strength of the non-contact adhesion  $f_a$  and we plot  $e$  against the impact velocity for different  $f_a$ . We observe that for  $f_a = 0$ ,  $e_n \approx 1$  at low velocities, while, for finite  $f_a$ , the particles stick to each other with  $e_n = 0$ . The critical velocity  $v_f^a$  required to separate the particles increases with  $f_a$ . For extreme values of  $f_a$  the particles stick in the whole range of velocities.

It is interesting to notice that for very low  $f_a$  and low impact velocities the behavior is independent of the adhesive force magnitude (cyan line and black circles lie on top of each other in Fig. 6). In the further sections we restrict our analysis to this range of  $f_a$  and impact velocity.

## 4 Elasto-plastic coefficient of restitution

In the following we will restrict our analytical study on the coefficient of restitution to the range of moderate and large impact velocity, where the contribution of weak non-

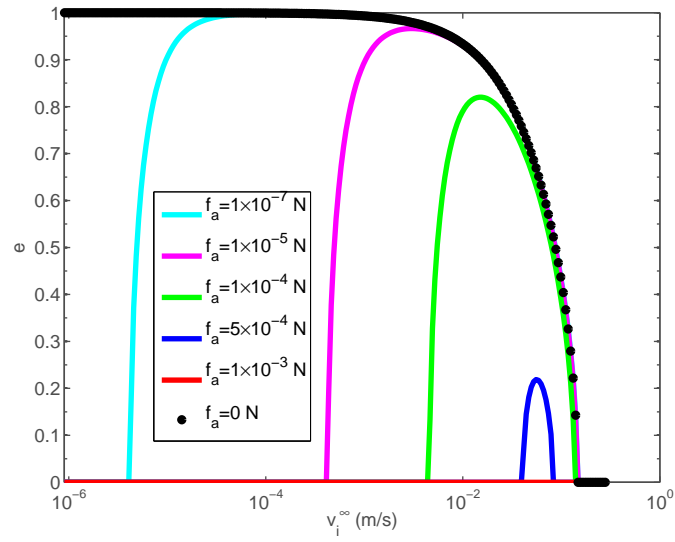


Figure 6: Restitution coefficient plotted as function of impact velocity without viscous dissipation. Different lines correspond to the analytical expression in Eq. (28) with different non-contact adhesion  $f_a$  as given in the inset. Black circles represent the numerical solution results for  $f_a = 0$ , where all other parameters are the same as in Fig. 5.

contact adhesive forces  $f_a \rightarrow 0$  can be neglected. Furthermore, we disregard viscous forces in order to allow for a closed analytical treatment. The coefficient of restitution will be computed and its dependence on the impact velocity  $v_i$  and the adhesive stiffness  $k_c$  is considered for two cases  $v_i < v_p$  and  $v_i \geq v_p$ , with  $v_p$  defined in Eq. (14).

## 4.1 Theory and dimensionless parameters

### 4.1.1 Initial relative velocity $v_i < v_p$

When  $v_i < v_p$  the particles after loading, unload with slope  $k_2$  and the system deforms along the path  $0 \rightarrow \delta_{\max} \rightarrow \delta_0 \rightarrow \delta_{\min} \rightarrow 0$ , as described in the Sec. 2.2.2 and shown in Fig. 2.

The initial kinetic energy (at  $\delta = 0$  overlap) is completely transformed to potential energy at the maximum overlap  $\delta_{\max}$ ,

$$\frac{1}{2}m_r v_i^2 = \frac{1}{2}k_1 \delta_{\max}^2 . \quad (22a)$$

The direction of relative velocity is reversed at  $\delta_{\max}$ , unloading starts with slope  $k_2$  and some part of the potential energy is converted to kinetic energy at the force-free overlap  $\delta_0$ ,

$$\frac{1}{2}m_r v_0^2 = \frac{1}{2}k_2 (\delta_{\max} - \delta_0)^2 , \quad (22b)$$

which, using Eq. (8), can be written as

$$\frac{1}{2}m_r v_0^2 = \frac{1}{2}k_1 \delta_{\max} (\delta_{\max} - \delta_0) . \quad (22c)$$

Further unloading, below  $\delta_0$ , leads to attractive forces. The kinetic energy at  $\delta_0$  is partly converted to potential energy at  $\delta_{\min}$

$$\frac{1}{2}m_r v_{\min}^2 + \frac{1}{2}k_2 (\delta_{\min} - \delta_0)^2 = \frac{1}{2}m_r v_0^2 . \quad (22d)$$

The total energy is finally converted to only kinetic energy at the end of the collision (overlap  $\delta = 0$ )

$$\frac{1}{2}m_r v_f^2 - \frac{1}{2}m_r v_{\min}^2 = -\frac{1}{2}k_c \delta_{\min}^2, \quad (22e)$$

that, when combined with (22d), gives

$$\frac{1}{2}m_r v_f^2 - \frac{1}{2}m_r v_0^2 = -\frac{1}{2}k_c \delta_{\min} \delta_0 \quad (22f)$$

Using Eqs. (22a), (22c), and (22f) with the definitions of  $\delta_{\min}$  and  $\delta_0$ , and dividing by the initial kinetic energy, we obtain the coefficient of restitution

$$e_n^{(1)} = \frac{v_f}{v_i} = \sqrt{\frac{k_1}{k_2} - \frac{k_c}{k_1} \frac{(k_2 - k_1)}{(k_2 + k_c)} \frac{(k_2 - k_1)}{k_2}} \quad (23)$$

with  $k_2 = k_2(\delta_{\max}) = k_2(v_i)$ , as defined in Eq. (10).

#### 4.1.2 Initial relative velocity $v_i \geq v_p$

When the initial relative velocity  $v_i$  is large enough such that  $v_i \geq v_p$ , the estimated maximum overlap  $\delta_{\max} = v_i \sqrt{m_r/k_1}$  is greater than  $\delta_{\max}^p$ . Let  $v_1$  be the velocity at overlap  $\delta_{\max}^p$ . The system deforms along the path  $0 \rightarrow \delta_{\max}^p \rightarrow \delta_{\max} \rightarrow \delta_0 \rightarrow \delta_{\min} \rightarrow 0$ , see Fig. 2. The initial relative kinetic energy is not completely converted to potential energy at  $\delta = \delta_{\max}^p$ , hence

$$\frac{1}{2}m_r v_i^2 = \frac{1}{2}m_r v_1^2 + \frac{1}{2}k_1 (\delta_{\max}^p)^2, \quad (24a)$$

and the loading continues with the slope  $k_p$  until all kinetic energy equals zero at  $\delta = \delta_{\max} > \delta_{\max}^p$

$$\frac{1}{2}m_r v_1^2 + \frac{1}{2}k_1 (\delta_{\max}^p)^2 = \frac{1}{2}k_p (\delta_{\max} - \delta_0)^2, \quad (24b)$$

the relative velocity changes sign at  $\delta_{\max}$ , the contact starts to unload with slope  $k_p$ . The potential energy is completely converted to kinetic energy at  $\delta_0$ , such that the equality

$$\frac{1}{2}m_r v_0^2 = \frac{1}{2}k_p(\delta_{\max} - \delta_0)^2 \quad (24c)$$

or

$$\frac{1}{2}m_r v_0^2 = \frac{1}{2}k_1 \delta_{\max}^p (\delta_{\max}^p - \delta_0) + \frac{1}{2}m_r v_1^2 \quad (24d)$$

holds. Further unloading, still with slope  $k_p$ , leads to attractive forces until  $\delta_{\min}^p$  is reached, where the kinetic energy is partly converted to potential energy

$$\frac{1}{2}m_r v_{\min}^2 + \frac{1}{2}k_p(\delta_{\min}^p - \delta_0)^2 = \frac{1}{2}m_r v_0^2. \quad (24e)$$

The unloading continues along  $k_c$  and the total energy at  $\delta_{\min}^p$  is finally converted to only kinetic energy at the end of collision ( $\delta = 0$  overlap), so that

$$\frac{1}{2}m_r v_f^2 - \frac{1}{2}m_r v_{\min}^2 = -\frac{1}{2}k_c(\delta_{\min}^p)^2. \quad (24f)$$

Using Eqs. (24c) and (24d) in Eq. (24f) gives

$$\frac{1}{2}m_r v_f^2 - \frac{1}{2}m_r v_0^2 = -\frac{1}{2}k_c \delta_{\min}^p \delta_0. \quad (24g)$$

Combining Eqs. (24a), (24b), (24c), (24g) with the definitions of  $\delta_{\min}^p$  and  $\delta_0$ , and dividing by the initial kinetic energy, we obtain the coefficient of restitution

$$e_n^{(2)} = \sqrt{1 + \left[ -1 + \frac{k_1}{k_p} - \frac{k_c}{k_1} \frac{(k_p - k_1)^2}{(k_p + k_c)k_p} \right] \frac{v_p^2}{v_i^2}}, \quad (25)$$

with  $v_p/v_i < 1$ .

### 4.1.3 Dimensionless Parameters

For a more general description, a few dimensionless parameters can be defined:

$$\text{Plasticity : } \eta = \frac{k_p - k_1}{k_1} , \quad (26a)$$

$$\text{Adhesivity : } \beta = \frac{k_c}{k_1} , \quad (26b)$$

$$\text{Scaled initial velocity : } \chi = \frac{\delta_{\max}}{\delta_{\max}^p} \sim \frac{v_i}{v_p} . \quad (26c)$$

The final dimensionless number, given here for the sake of completeness, but not used in this subsection, is the ratio of maximum velocity at which particles stick due to adhesion only to the initial relative velocity of the particles.  $\psi_a = v_a/v_i^\infty \ll 1$ .

Using Eqs. (26a), (26b) and (26c) in Eq. (10), one can define

$$k_2(\chi) = \begin{cases} k_p & \text{if } \chi \geq 1 \\ k_1(1 + \eta\chi) & \text{if } \chi < 1 \end{cases} , \quad (27)$$

while the coefficients of restitution,  $e_n^{(1)}$  in Eq. (23) and  $e_n^{(2)}$  in Eq. (25) become

$$e_n^{(1)}(\eta, \beta, \chi < 1) = \sqrt{\frac{1}{1 + \eta\chi} - \frac{\beta\eta^2\chi^2}{(1 + \eta\chi)(1 + \beta + \eta\chi)}} \quad (28)$$

and

$$e_n^{(2)}(\eta, \beta, \chi \geq 1) = \sqrt{1 + [A(\eta, \beta) - 1] \frac{1}{\chi^2}} , \quad (29)$$

with

$$A(\eta, \beta) = \left[ e_n^{(1)}(\eta, \beta, \chi = 1) \right]^2 . \quad (30)$$

### 4.1.4 Qualitative Description

In Fig. 7, the analytical prediction for the coefficient of restitution, from Eqs. (28) and (29), is compared to the numerical integration of the contact model, for different

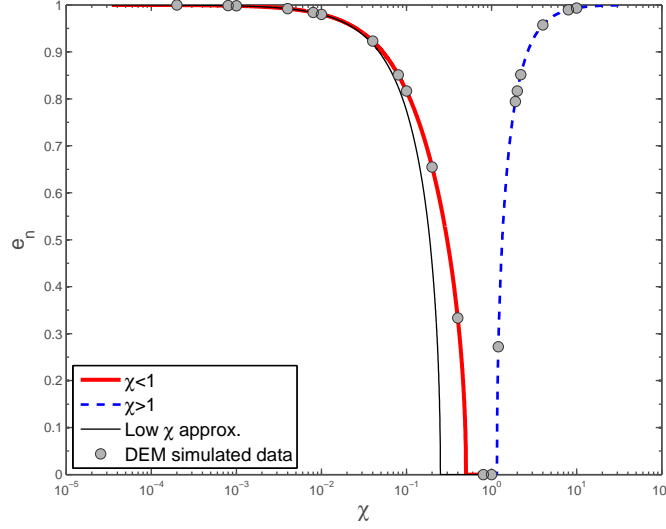


Figure 7: Restitution coefficient plotted as a function of the scaled initial velocity  $\chi$  for a collision without viscous and non-contact forces. The thick red line correspond to the analytical expressions in Eq. (28), the dashed blue line to Eq. (29), and circles are DEM simulations, while the thin black line represents the low velocity approximation results for the same material parameters as in Fig. 5, i.e.  $\eta = 4$  and  $\beta = 1$ .

scaled initial velocities  $\chi$ . We confirm the validity of the theoretical prediction for the coefficient of restitution in the whole range.

For very small  $\eta\chi < 10^{-3}$ ,  $e_n$  can be approximated as  $e_n^{(1)} \approx 1 - \frac{\eta\chi}{2}$ , which gives a good agreement to 2 orders of magnitude in velocity. With increasing initial relative velocity  $v_i$ , dissipation increases faster than the initial kinetic energy leading to a faster convex decrease of  $e_n^{(1)}$ . The coefficient of restitution  $e_n^{(1)}$  becomes zero when a critical scaled initial velocity  $\chi_c^{(1)}$  (see Eq. (32)) is reached. At this point, the amount of dissipated energy is equal to the initial kinetic energy, leading the particles to stick. The coefficient of restitution remains zero until a second critical scaled initial velocity  $\chi_c^{(2)}$  is reached, i.e. sticking behavior is observed for  $\chi_c^{(1)} \leq \chi \leq \chi_c^{(2)}$ . Finally, for  $\chi > \chi_c^{(2)}$ , the dissipated energy remains constant (plastic limit is reached), while the initial kinetic energy increases. As a result, the kinetic energy after collision increases and so does the coefficient of restitution  $e_n$ . Existence of sticking at such high velocities is



recently reported by Kothe et al. [23], where authors studied the outcome of collisions between sub-mm-sized dust agglomerates in micro-gravity.<sup>1</sup> The increase in  $e_n$  with the velocity is because of a limit on maximum plastic overlap, thereby making the plastic dissipation to be constant for  $\delta > \delta_{\max}^p$ .

Certainly, this is in contrast to what is expected and observed in experiments on some types of elasto-plastic granular materials. We point out that this behavior shows up only at very high velocities (x-axis in Fig. 7 has increased by 2 orders of magnitude). Moreover, the definition of  $e_n$  might become questionable at that high velocity, as the particles can fragment/break and physics of the system has to be reconsidered. At such large deformations the particles cannot be assumed to be spherical anymore. On the other hand, the increase of  $e_n$  for high velocity is a familiar observation in the cold spray community [43, 60, 71]. After a given (critical) velocity the spray particles adhere to the substrate, and they do so for a range of impact velocities, while increasing velocity further leads to unsuccessful deposition, i.e. the particles will bounce from the substrate. The sticking phenomenon of the material has been extensively studied experimentally and numerically [43, 60, 70, 71, 74].

As explained in the previous section 2.2.3, a pre-determinate threshold  $\delta_{\max}^p$  on the plastic regime is the reason for the anomalous elastic high velocity behavior of the coefficient of restitution. The model can be tuned by choosing a higher  $\phi_f$ , recalculating  $k_p$ , thereby keeping the behavior plastic in the whole range of interest for the velocity and the collision dynamics up to  $\delta_{\max}^p$  unchanged (see appendix B). Nevertheless, we consider a reference value for  $\phi_f$  (and  $k_p$ ) based on the maximum volume fraction of the multi-particle granular assembly, such that the macroscopic behavior is reasonable and in good agreement with the experiment, e.g. based on our simulations on split-bottom ring shear cell [30]. Also, in a typical DEM simulation, the maximum overlap is 5 – 10% of the reduced particle radius. This is illustrated in Fig. 8, where

---

<sup>1</sup>Note that this is the regime where the physics of the contact changes and dependent on the material and other considerations, modifications to the contact model could/should be applied, however, this goes beyond the scope of this paper.

we plot  $e_n$  against the normalized velocity  $\chi = \frac{v_i}{v_p}$ , for different values of  $\phi_f$ , with  $v_p$  calculated from the same reference stiffness input parameters  $\phi_f$  and  $k_p$ . Reference  $\phi_f$  is chosen to be 0.05, which would mean  $\delta_0^p = 0.05a$ . For low velocity the different curves lie on the top of each other, showing that the collision dynamics stays unaffected by the change in  $\phi_f$ . The onset of the increase in  $e_n$  shifts to right with increasing  $\phi_f$ , providing a fully plastic regime at high  $\chi$  if desired.

In Fig. 9, we compare the variation of the force with overlap in the various regimes of  $\chi$  as discussed above for  $\phi_f = 0.05$ . For very small  $\chi$ , the unloading slope  $k_2 \approx k_1$ , (see Fig. 9(a) for a moderately small  $\chi = 0.34$ ), and the amount of dissipated energy is small, increasing with  $\chi$ . The kinetic energy after collision is almost equal to the initial kinetic energy, i.e.  $e_n \sim 1$ , see Fig. 7. In Figs. 9(b) and 9(c), the force-overlap variation is shown for sticking particles, for the cases  $\chi_c^{(1)} < \chi < 1$  and  $1 < \chi < \chi_c^{(2)}$ , respectively (more details will be given in the following subsection). Finally, in Fig. 9(d), the case  $\chi > \chi_c^{(2)}$  is displayed, for which the initial kinetic energy is larger than the dissipation, resulting in the separation of the particles. The corresponding energy variation is described in detail in the appendix.

#### 4.1.5 Sticking regime limits and overlaps

In this section we focus on the range of  $\chi_c^{(1)} < \chi \leq \chi_c^{(2)}$ , where the particles stick to each other and calculate the critical values  $\chi_c^{(1)}$  and  $\chi_c^{(2)}$ . Also we assume  $\beta$  to be large enough so that sticking is possible, as we show in later section that for a given  $\eta$  a minimum  $\beta = \beta^*$  is required for particles to stick. When  $\chi = \chi_c^{(1)}$  all initial kinetic energy of the particles is dissipated during the collision. Hence the particles stick and  $e_n$  becomes zero:

$$e_n^{(1)}(\eta, \beta, \chi_c^{(1)}) = 0, \quad (31a)$$

which leads to

$$\beta \eta^2 \chi^2 - \eta \chi - (1 + \beta) = 0. \quad (31b)$$

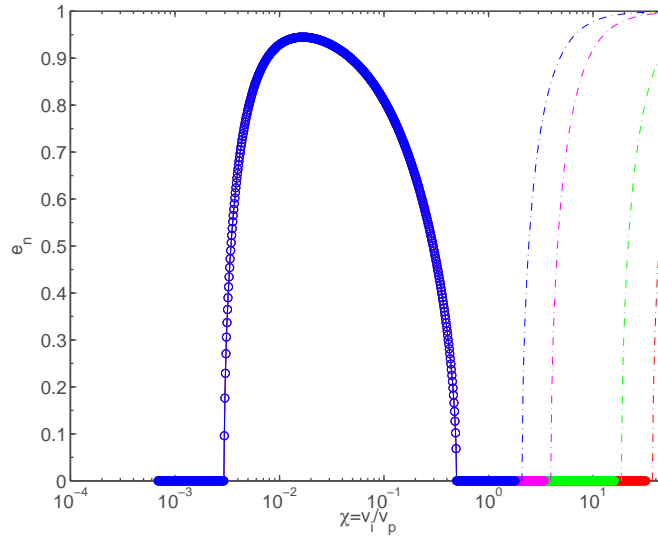


Figure 8: Restitution coefficient plotted as a function of the scaled initial velocity  $\chi$ . The blue solid line corresponds to the solution for  $\chi < 1$ , with  $\phi_f = 0.05$ , while the dashed lines with different colors represent the behavior once limit overlap is reached. Magenta, green and red represent  $e_n$  for  $\phi_f' = 0.1$ ,  $\phi_f' = 0.5$  and  $\phi_f' = 1.0$  respectively, where the latter is the fully plastic case, as if one would set  $\delta_0^p = a$ , where  $a$  is the particle radius. Note that  $k_p$  is adapted as described in appendix B.

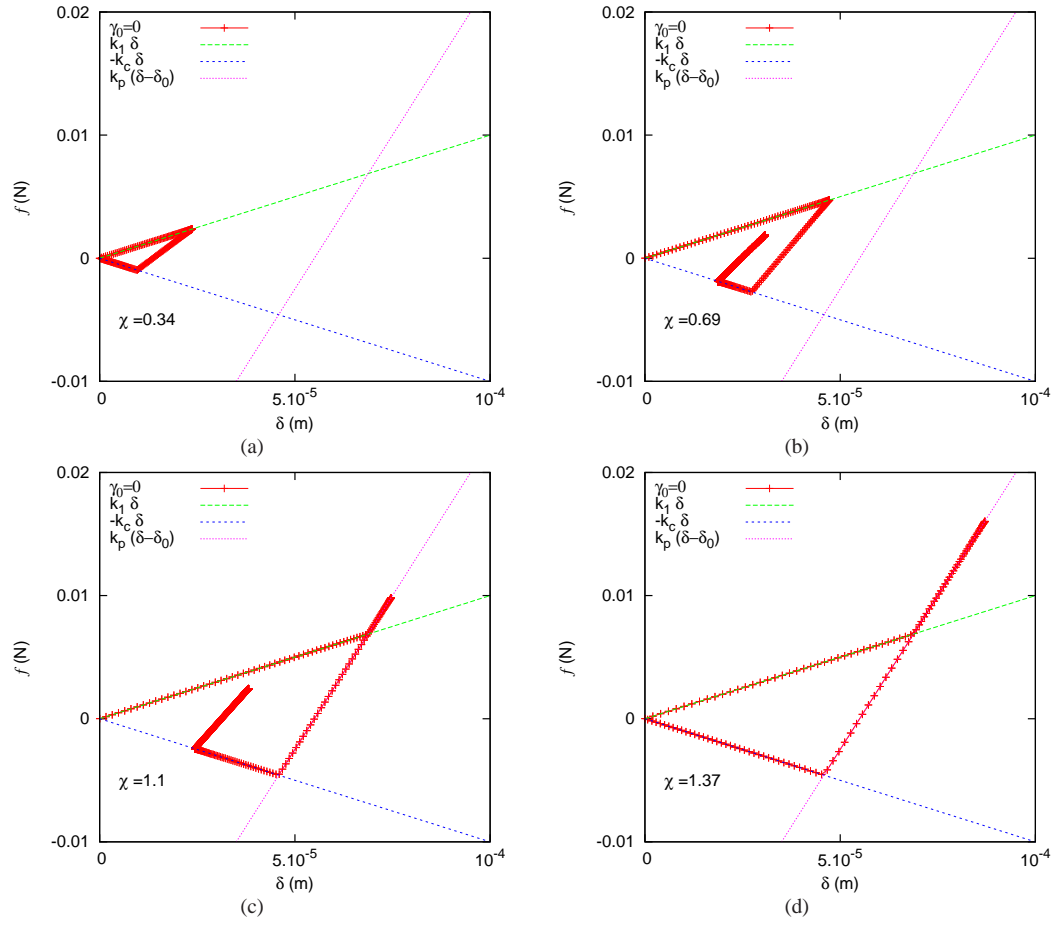


Figure 9: Contact force during one collision, plotted against the overlap for different scaled initial velocities  $\chi = 0.34, 0.69, 1.1$ , and  $1.37$ , respectively. The three straight lines represent the plastic branch, with slope  $k_1$ , the adhesive branch, with slope  $-k_c$ , and the limit branch with slope  $k_p$ , for  $k_1 = 10^2 \text{ Nm}^{-1}$ ,  $k_p = 5 \times 10^2 \text{ Nm}^{-1}$ ,  $k_c = 10^2 \text{ Nm}^{-1}$  and  $\phi_f = 0.05$ , i.e.  $\eta = 4$  and  $\beta = 1$

Only the positive  $\chi$  solution is physically possible, as particles with negative initial relative velocity cannot collide, so that

$$\chi_c^{(1)} = \frac{1}{2\beta\eta} \left[ 1 + \sqrt{1 + 4\beta(1 + \beta)} \right]. \quad (32)$$

For larger  $\chi > \chi_c^{(1)}$ , the dissipation is strong enough to consume all the initial kinetic energy, hence the particles loose kinetic energy at a positive, finite overlap  $\delta_c$ , see Fig. 9(b). The contact deforms along the path  $0 \rightarrow \delta_{\max} \rightarrow \delta_0 \rightarrow \delta_{\min} \rightarrow \delta_c$ . Thereafter, in the absence of other sources of dissipation, particles keep oscillating along the same slope  $k_2$ . In order to compute  $\delta_c$ , we use the energy balance relations in Eqs. (22), and conservation of energy along  $\delta_{\min} \rightarrow \delta_c$ , as described by Eq. (22e)

$$\frac{1}{2}m_r v_f^2 - \frac{1}{2}m_r v_0^2 = -\frac{1}{2}k_c \left\{ \delta_{\min} \delta_0 - \frac{1}{2}k_c \delta_c^2 \right\}, \quad (33a)$$

with  $v_f = 0$  at the overlap  $\delta_c$ . Re-writing in terms of  $k_c$  and  $\delta_{\max}$  leads to

$$k_c \delta_c^2 + \left\{ \frac{k_1^2}{k_2} - \frac{k_c(k_2 - k_1)^2}{k_2(k_2 + k_c)} \right\} \delta_{\max}^2 = 0 \quad (33b)$$

and thus to the sticking overlap

$$\frac{\delta_c^{(1)}}{\delta_{\max}^p} = \frac{\delta_{\max}}{\delta_{\max}^p} \sqrt{\frac{(k_2 - k_1)^2}{k_2(k_2 + k_c)} - \frac{k_1^2}{k_2 k_c}}. \quad (33c)$$

In terms of dimensionless parameters, as defined earlier, one gets

$$\frac{\delta_c^{(1)}}{\delta_{\max}^p} = \chi \sqrt{\frac{\eta^2 \chi^2}{(1 + \eta\chi)(1 + \beta + \eta\chi)} - \frac{1}{\beta(1 + \eta\chi)}} = \frac{\chi}{\sqrt{\beta}} |e_n^{(1)}|, \quad (34)$$

where  $|e_n^{(1)}|$  denotes the absolute value of the result from Eq. (28).

For larger initial relative velocities,  $\chi \geq 1$ , the coefficient of restitution is given by

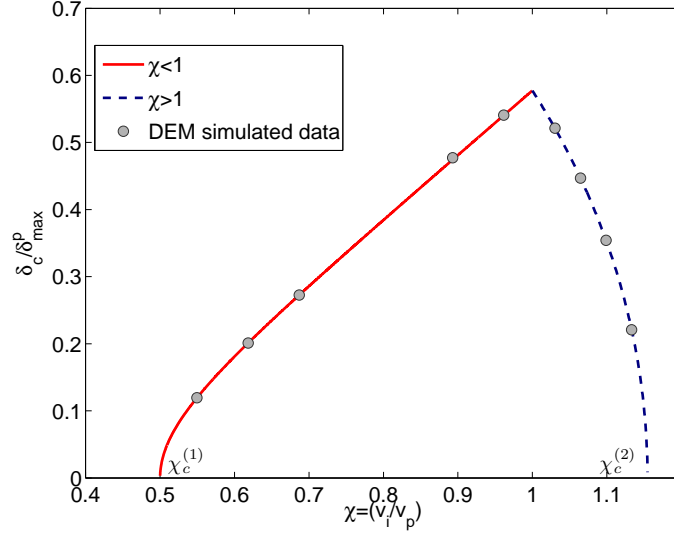


Figure 10: Kinetic energy-free contact overlap  $\delta_c$  plotted as a function of the scaled initial velocity  $\chi = \frac{v_i}{v_p}$ ; the increasing branch corresponds to  $\chi < 1$ , while the decreasing branch corresponds to  $\chi > 1$ . The dots are simulations for  $\eta = 4$  and  $\beta = 1$ , as in Fig. 9, which yields  $\delta_c^{\max} / \delta_{\max}^p = (1/3)^{1/2}$  in Eq. (39).

Eq. (29), so that the second critical  $1 < \chi_c^{(2)}$  can be computed setting

$$e_n^{(2)}(\eta, \beta, \chi_c^{(2)}) = 0, \quad (35a)$$

or

$$\left[ \frac{1}{1+\eta} - \frac{\beta\eta^2}{(1+\eta)(1+\beta+\eta)} - 1 \right] \frac{1}{\chi^2} = 1. \quad (35b)$$

Again, only the positive solution is physically possible, so that

$$\chi_c^{(2)} = \sqrt{1 - \frac{1}{1+\eta} + \frac{\beta\eta^2}{(1+\eta)(1+\beta+\eta)}} \quad (36)$$

is the maximum value of  $\chi$  for which particles stick to each other. For  $\chi \leq \chi_c^{(2)}$  particles deform along the path  $0 \rightarrow \delta_{\max}^p \rightarrow \delta_{\max} \rightarrow \delta_0 \rightarrow \delta_{\min} \rightarrow \delta_c$  and then keep oscillating with  $k_2$  stiffness,  $\delta_c$  being one of the extrema of the oscillation, see Fig.

9(c). From Eq. (24e), applying conservation of energy along  $\delta_{\min} \rightarrow \delta_c$ , we get

$$\frac{1}{2}m_r v_f^2 - \frac{1}{2}m_r v_0^2 = -\frac{1}{2}k_c \delta_{\min} \delta_0 + \frac{1}{2}k_c \delta_c^2, \quad (37a)$$

with  $v_f = 0$ , and re-writing in terms of  $k_c$  and  $\delta_{\max}^p$  leads to

$$\frac{\delta_c^{(2)}}{\delta_{\max}^p} = \sqrt{\left[ \frac{(k_p - k_1)^2}{k_p(k_p + k_c)} - \frac{k_1^2}{k_c k_p} + \frac{k_1}{k_c} \right] - \frac{m_r}{k_c} \frac{v_i^2}{(\delta_{\max}^p)^2}}. \quad (37b)$$

In terms of the dimensionless parameters, this yields

$$\frac{\delta_c^{(2)}}{\delta_{\max}^p} = \sqrt{\frac{\eta^2}{(1+\eta)(1+\beta+\eta)} + \frac{\eta}{\beta(1+\eta)} - \frac{\chi^2}{\beta}} = \frac{\chi}{\sqrt{\beta}} |e_n^{(2)}|, \quad (38)$$

where  $|e_n^{(2)}|$  denotes the absolute value of the result from Eq. (29).

In Fig. 10, the evolution of  $\delta_c/\delta_{\max}^p$  with  $\chi$  is reported, showing perfect agreement of the analytical expressions in Eqs. (34) and (38), with the numerical solution of a pair-collision. In the sticking regime, the stopping overlap increases with  $\chi$ , and reaches a maximum at  $\chi = 1$ ,

$$\delta_c^{\max}/\delta_{\max}^p = \sqrt{\frac{\beta\eta^2 - \eta - \beta - 1}{\beta(1+\eta)(1+\eta+\beta)}} \quad (39)$$

which depends on the the adhesivity  $\beta$  and the plasticity  $\eta$  only. For  $\chi > 1$ , dissipation gets weaker, relatively to the increasing initial kinetic energy, and  $\delta_c^{(2)}/\delta_{\max}^p$  decreases until it reaches 0 for  $\chi = \chi_c^{(2)}$ .

## 4.2 Dependence on Adhesivity $\beta$

In the previous subsections, we studied the dependence of the coefficient of restitution  $e_n$  on the scaled initial velocity  $\chi$  for fixed adhesivity  $\beta$ , whereas here the dependence of  $e_n$  on  $\beta$  is analyzed.

A special adhesivity  $\beta^*$  can be calculated such that  $e_n = 0$  for  $\chi = 1$ , which is the case of maximum dissipation and leads to sticking only at exactly  $\chi = 1$ . From Eq. (28), we get

$$1 + \beta^* + \eta - \beta^* \eta^2 = 0 , \quad (40a)$$

so that

$$\beta^* = \frac{1}{\eta - 1} . \quad (40b)$$

In Fig. 11, we plot the coefficient of restitution as function of the scaled initial velocity  $\chi$  for different values of adhesivity  $\beta$ . For  $\beta < \beta^*$ , in Fig. 11, the coefficient of restitution  $e_n$  decreases with increasing  $\chi < 1$ , reaches its positive minimum at  $\chi = 1$ , and increases for  $\chi > 1$ . In this range, the particles (after collision) always have a non-zero relative separation velocity  $v_f$ . When  $\beta = \beta^*$ ,  $e_n$  follows a similar trend, becomes zero at  $\chi = 1$ , and increases with increasing scaled initial velocity for  $\chi > 1$ . This is the minimum value of adhesivity for which  $e_n$  can become zero and particles start to stick to each other. For  $\beta = \beta^*$ , the two critical values coincide,  $\chi_c^{(1)} = \chi_c^{(2)} = 1$ . If  $\beta > \beta^*$ ,  $e_n$  decreases and becomes zero at  $\chi = \chi_c^{(1)} < 1$ , it remains zero until  $\chi = \chi_c^{(2)} > 1$ , and from there increases with increasing initial velocity. Hence, we can conclude that the sticking of particles and then range of velocity for which this happens, is affected by material properties of both particles. Indeed Zhou et al. [74] presented similar conclusion about deposition efficiency in cold spray.

### 4.3 Effect of Viscosity

Since real physical systems also can have additional dissipation modes that are, e.g., viscous in nature, in this section we study the behavior of the collision when viscosity is present ( $\gamma_0 > 0$ ) and compare it with the non-viscous case ( $\gamma_0 = 0$ ). Note that any non-linear viscous damping force can be added to the contact laws introduced previously, however, for the sake of simplicity we restrict ourselves to the simplest linear viscous



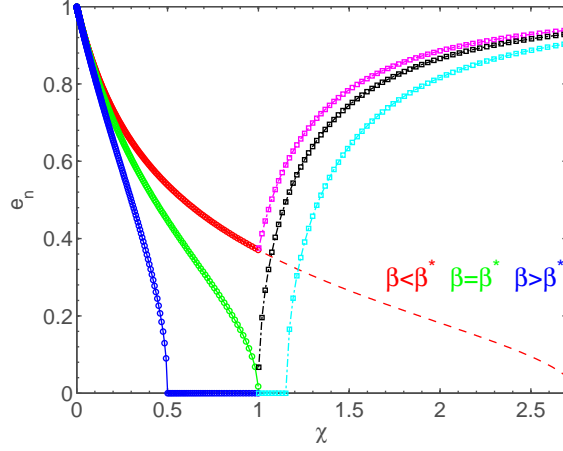


Figure 11: Coefficient of restitution  $e_n$  plotted against the scaled initial velocity  $\chi$ . Circles with different colors correspond to different adhesivity  $\beta$  (red for  $\beta < \beta^*$ , green for  $\beta = \beta^*$  and blue for  $\beta > \beta^*$ ) for  $\chi \leq 1$ , while magenta, black and cyan squares correspond to the respective values of  $\beta$  for  $\chi > 1$ . Other parameters used are  $k_1 = 10^2$ ,  $k_p = 5 \times 10^2$ , and different  $k_c$  (all in units of  $\text{Nm}^{-1}$ ), i.e.  $\eta = 4$  and  $\beta/\beta^* = 1/3, 1$ , and  $3$ , with  $\beta^* = 1/3$ . The dashed red line represents the solution with the tuned fully plastic model with a new  $\phi_f' = 0.5$  and newly calculated  $k_p'$ , see Appendix B.

law as given as second term in Eq. (3). However it is important to choose the correct viscous damping term for the force law to get the correct behavior as explained in [24,27,32,66]. In Fig. 12, we plot the contact force against the overlap, and the overlap against time, during collisions for a constant value of  $\chi = 1$  and different  $\beta$ , for  $\gamma_0 = 5 \times 10^{-3}$ .

When  $\beta < \beta^*$ , see Fig. 12(a) and Fig. 12(b), the contact ends when the adhesive force  $-k_c \delta$  goes back to zero, for both cases, with and without viscosity. This is since the viscosity is relatively small and does not contribute enough to the total dissipation to make the particles stick.

For the critical adhesivity  $\beta = \beta^*$ , reported in Fig. 12(c), without viscosity the overlap between the particles still goes down to exactly zero at the end of the collision, with all kinetic energy dissipated. For  $\gamma_0 > 0$ , dissipation brings this marginal collision case into the sticking regime and the particles stay in contact at  $\delta > 0$ . This can be

seen clearly in Fig. 12(d), where the particles undergo a damped oscillatory motion with amplitude depending on the residual velocity  $v_f$  (the amplitude is very small due to small residual velocity).

For larger values  $\beta > \beta^*$ , the overlap does not reach 0, neither for  $\gamma_0 = 0$  nor for  $\gamma_0 > 0$ , see Fig. 12(e). In both cases, the particles stick and remain in contact with a finite overlap. Without viscosity, the particles keep oscillating along the slope  $k_2$ , while in the case with viscosity the oscillation is damped and kinetic energy vanishes. During loading and unloading the apparent slope changes with time due to the additional viscous force that leads to the dissipation of energy. Waiting long enough, for some oscillation cycles, the particles stick to each other with a finite overlap and zero relative kinetic energy. The difference is displayed in Fig. 12(f), where for  $\gamma_0 = 0$  the particles keep oscillating with constant amplitude, whereas, for  $\gamma_0 > 0$ , the particles undergo a damped oscillatory motion, until the velocity becomes 0 at  $\delta > 0$ . The time evolution of the overlap in Fig. 12(f) resembles that of the displacement evolution in Ref. [13], where the authors studied sticking of particles in Saturn's rings.<sup>2</sup>

#### 4.4 Asymptotic Solutions

In this subsection, we focus on the case  $\chi \leq 1$ , and study the asymptotic behavior of the coefficient of restitution as function of the impact velocity.

For the sake of simplicity, let us start with an elasto-plastic system without adhesion, i.e.  $k_c = 0$ , in Eq. (28) such that

$$e_n^{(1)}(\eta, \beta = 0, \chi < 1) = \sqrt{\frac{1}{1 + \eta\chi}}, \quad (41a)$$

---

<sup>2</sup>In general, one could add a viscous law that is proportional to  $k_2 - k_1$  or to a power of overlap  $\delta$ , such that the jump-in viscous force in (e) at the beginning of the contact is not there, however, we do not go into this detail.

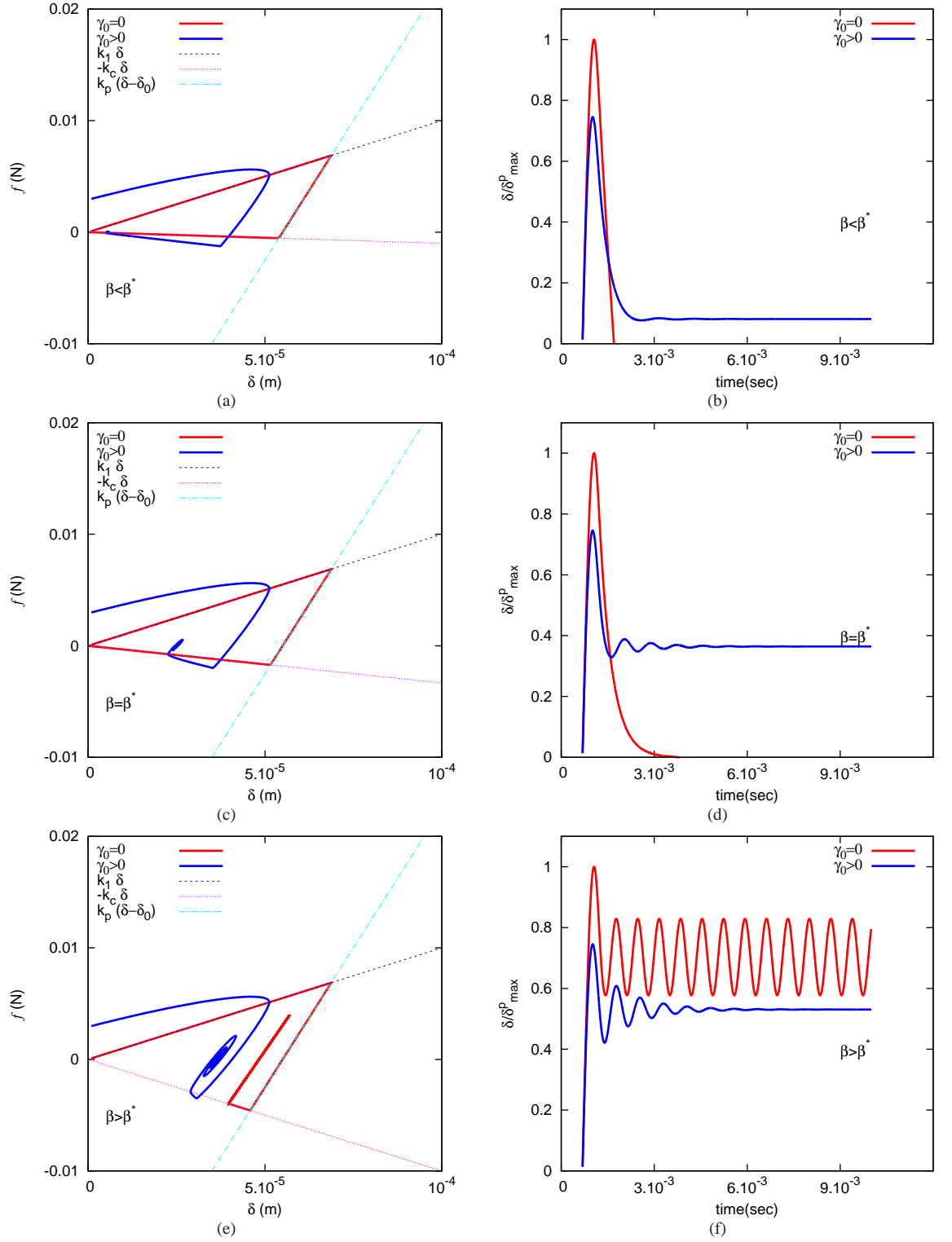


Figure 12: (a), (c), (e) Contact forces plotted against overlap and (b), (d), (f) time evolution of  $\delta/\delta_{\max}^p$  for pair collisions with parameters  $k_1 = 10^2$ ,  $k_p = 5 \times 10^2$  and different  $k_c = 10, 33.33$ , and  $100$ , (units  $\text{Nm}^{-1}$ ), i.e. with  $\eta = 4$ ,  $\beta < \beta^*$ ,  $\beta = \beta^*$  and  $\beta > \beta^*$ , for the same situations as shown in Fig. 11. The red and blue lines represent the data in the presence and absence of viscosity respectively, where  $\gamma_0 = 5 \times 10^{-3}$ , (unit  $\text{Nm}^{-1}\text{sec}$ ).

inserting the definitions of  $\eta$ ,  $\beta$  and  $v_p$ ,

$$e_n^{(1)}(\beta = 0, v < v_p) = \sqrt{\frac{1}{1 + \frac{k_p - k_1}{k_1} \frac{v_i}{\sqrt{\frac{2k_1}{m}} \delta_{\max}^p}}}, \quad (41b)$$

using Eq. (13), where we defined  $S = \frac{k_p - k_1}{k_1 \delta_{\max}^p}$  and assuming  $\omega_o = \sqrt{\frac{2k_1}{m}}$ , we get

$$e_n^{(1)}(\beta = 0, v < v_p) = \sqrt{\frac{1}{1 + \frac{Sv_i}{\omega_o}}}. \quad (41c)$$

Eq. (41c) is exactly the same as Eq. (5) in [68]. For non-cohesive particles, and in the range  $v < v_p$  we get exactly the same solution as Walton and Braun [68].

Further to study the asymptotic solution

$$e_n^{(1)}(\eta, \beta = 0, \chi < 1) = \sqrt{\frac{1}{1 + \eta\chi}} \approx (\eta\chi)^{-1/2} \quad (42)$$

with the approximation valid for  $\eta\chi \gg 1$ . Since the scaled velocity is moderate,  $\chi < 1$ , the condition requires a large plasticity, i.e., a strong difference between the limit stiffness and the plastic loading stiffness,  $\eta \gg 1$  (or  $k_p \gg k_1$ ). In Fig. 13, we plot the coefficient of restitution against the scaled initial velocity  $\chi$  for three different values of  $\eta = k_p/k_1$ , together with the power law prediction of Eq. (42). We observe, that for the smallest  $\eta$  (red circle and line), the approximation is far from the data, while for higher  $\eta$ , the approximation works well even for rather small velocities  $\chi \approx 0.1$ .

Next, when studying the elasto-plastic adhesive contact model,  $\beta > 0$  and  $\beta \ll 1$ , again, we restrict ourselves to values of  $\eta$  such that asymptotic condition  $\eta\chi \gg 1$  is satisfied. Hence, Eq. (28) can be approximated as

$$e_n^{(1)}(\eta, \beta, \chi < 1) \approx \sqrt{\frac{1}{\eta\chi} - \beta}, \quad (43)$$

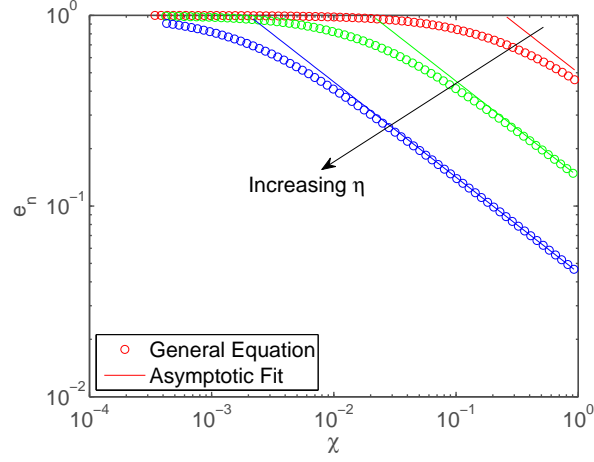


Figure 13: The coefficient of restitution is plotted against the scaled initial velocity  $\chi$  in log-log-scale for  $\beta = 0$  and three values of  $\eta = 5, 50$ , and  $500$ , with the other parameters as in Fig. 7. Red, green and blue circles denote, respectively, the solution of Eq. (42), while the solid lines represent the approximation for high scaled impact velocity and large plasticity  $\eta \gg 1$ .

as long as  $\eta\chi \gg \beta \geq 0$  and  $\frac{1}{\eta} > \beta$  holds.

In Fig. 14, we plot the coefficient of restitution against the scaled initial velocity  $\chi$  for different values of  $\beta$  and superimpose the approximation, Eq. (43). For small  $\beta$  and large  $\chi$ , one observes good agreement between the full solution and the approximation. Differently, for the highest values of  $\beta$  the approximation is not valid. Due to the adhesive force, for large  $\chi$ , with increasing  $\beta$ , the deviation from the  $\chi^{-1/2}$  power law becomes increasingly stronger, leading to the sticking regime, as discussed in the previous subsections. On the other hand, for smaller velocities, one observes a considerably smaller power-law, resembling the well-known  $\chi^{-1/4}$  power law for plastic contacts, as indicated by the dashed line in Fig. 14.

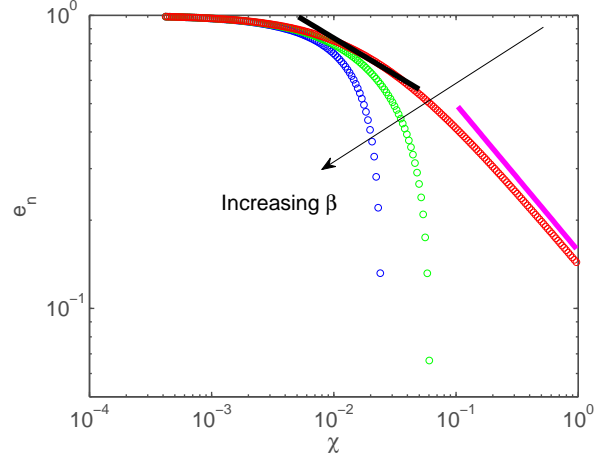


Figure 14: Log-log plot of the coefficient of restitution against the scaled initial velocity  $\chi$  for four different values of  $\beta = 0.01, 0.1$ , and  $1.0$ , with  $\eta = 50$ . Red, green and blue circles denote the respective solutions of the general equation, Eq. (28), solid black line represents power law  $e_n \sim \chi^{-1/4}$ , while magenta line denotes  $e_n \sim \chi^{-1/2}$ .

#### 4.5 Dependence on interpolation

The choice of the interpolation rule for the unloading stiffness  $k_2$  in Eq. (27) is empirical. Therefore, for  $\delta_{\max}/\delta_{\max}^p < 1$ , a different choice could be:

$$k_2(\delta_{\max}) = k_1(1 + \eta\sqrt{\chi}). \quad (44)$$

Inserting Eq. (44) into Eq. (23) leads to a different expression for the normal coefficient of restitution  $e_n^{(1)}$ , which for high values of  $\eta\sqrt{\chi}$ , and for small  $\beta$ , reduces to

$$e_n \propto \sqrt{\eta}(\chi)^{-1/4}. \quad (45)$$

A similar power law prediction for moderate velocities has been previously obtained by Thornton et al. in Ref. [52], using a non-linear Hertzian loading and unloading. Fig. 15 shows the agreement between the power law approximation  $\chi^{-1/4}$  and Eq. (23) with the alternative interpolation rule (44), for moderate velocities. The choice of different

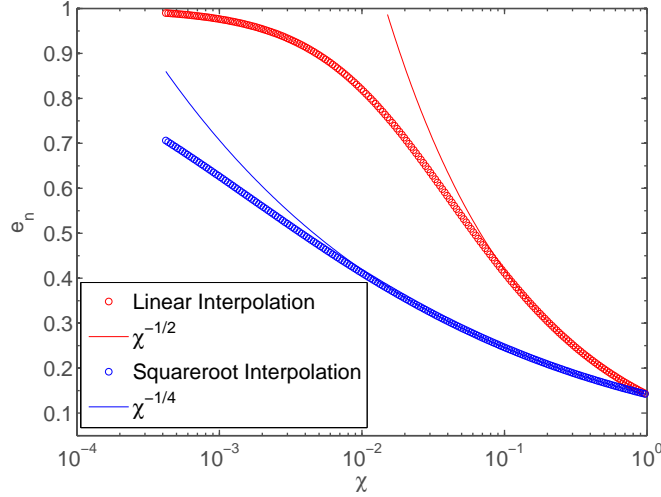


Figure 15: Semi-log plot of the coefficient of restitution as function of the scaled initial velocity  $\chi$ , using different interpolation rules for  $k_2$ , for pair collisions with  $\eta = 50$  and  $\beta = 0$ . The symbols denote the solutions of the general equation, Eq. (42) with linear interpolation (red circles) or square root interpolation (blue circles), as given in Eq. (44). The red and blue solid lines represent the approximations for high impact velocity  $e_n \sim \chi^{-1/2}$  and  $e_n \sim \chi^{-1/4}$ .

interpolation laws for  $k_2$  shows the flexibility of the model and requires input from experiments to become more realistic. The convexity of linear interpolation for zero cohesion is very similar to that of low  $\beta$  in Fig. 11.

## 5 Conclusions

Various classes of contact models for non-linear elastic, adhesive and elasto-plastic particles, are reviewed in this paper. Instead of considering the well understood models for perfect spheres of homogeneous (visco) elastic or elasto-plastic materials, here we focus on a special class of mesoscopic adhesive elasto-plastic models, aimed to describe the overall behavior of assemblies of realistic (different from perfectly homogeneous spheres) fine particles.

The contact model by Luding [29] is extended and generalized by adding short-

ranged (non-contact) interactions. The model is critically discussed and compared to alternative approaches which are classified in Sub-Section 1.2. The influence of the model parameters on the overall impact behavior is discussed, focusing on the irreversible, adhesive, elasto-plastic part of the model and combining all the elements (non-contact, hysteretic, contact and viscous dissipation) at the end. The model is simple yet it catches the important features of particle interactions that affect the bulk behavior of a granular assembly, like elasticity, plasticity and contact adhesion. It is mesoscopic in spirit, i.e. it does not resolve all the details of every single contact, but it is designed to represent the ensemble of many contacts in a bulk system. The goal is to propose a rich, flexible and multi-purpose granular matter model, which is realistic and allows to involve large numbers of particles.

When the dependence of the coefficient of restitution,  $e$ , on the relative velocity between particles is analyzed, two sticking regimes,  $e = 0$ , show up. These are related to different sources of dissipation in the system.

(i) As previously reported in the literature (see e.g. Refs. [4, 9, 17, 44, 52]) the particles stick to each other at very low impact velocity. This can happen due to irreversible short-range non-contact interaction. The threshold velocity, below which the particles stick, is directly related to the magnitude of the non-contact adhesive force  $f_a$ . (ii) With increasing velocity,  $e$  increases and then decreases until the second sticking regime is reached. This is a result of the plastic/adhesive dissipation mechanisms in the hysteretic contact model.

At small impact velocity, the details of the contact model are of minor importance. At higher velocities, for a sufficiently low value of jump-in force  $f_a$  the contribution of the (irreversible) non-contact forces can be neglected. In the limit of weak  $f_a$  and for moderate-high velocities, the contact component of the coefficient of restitution  $e_n$  is examined analytically using simple energy conservation arguments.

The results are derived in a closed analytical form, by phrasing the behavior in



terms of dimensionless parameters (plasticity, adhesivity and initial velocity) and the range of impact velocities of the second sticking regime is predicted.

For still increasing relative velocity, beyond the sticking region,  $e_n$  starts increasing again. This regime involves a change of the physical behavior of the system and resembles for example material with an elastic core like asphalt (stone with bitumen layer). Completely plastic behavior can be reproduced by the same model without any change, just by tuning two input parameters  $k_p$  and  $\phi_f$ , such that low velocity collision dynamics is kept unaffected but the maximal plastic overlap is reached only at much higher impact velocities. This modification provides the high velocity sticking regime for high velocity, as expected for plastic material. The existence of a high velocity rebound, as predicted by our model, has been observed experimentally and numerically in cold spray [43, 60, 70, 71, 74] and can be expected for elastic core with a thin plastic shell. As shown in appendix B, the model is flexible enough to model the “unusual” behavior (which might be relevant to other applications described above), as well as the well-known decrease of the coefficient of restitution with impact velocity.

In the sticking regime, due to the lack of dissipation on the unloading / re-loading branch the sticking particles oscillate around their equilibrium position. However, the real collision between two-particles is dissipative in nature. Since viscosity hinders analytical solutions, a few simulation results with viscosity are presented. With viscosity, the unloading/re-loading is not reversible elastic anymore. Thus with time the particles undergo a damped oscillation and approach a static contact with finite overlap.

In the last part of the paper a section is dedicated to the asymptotic behavior of  $e_n$  at high impact velocities. We observe that the asymptotic behavior is directly related to the choice of the interaction law and its details. For low adhesivity, the coefficient of restitution is found to decay as  $e_n \sim v_i^{-1/2}$ , which is due to the empirical choice of the unloading stiffness in the model. Further analysis on this feature is possible in the future, when new data from modern experimental techniques involving fine powders or

core-shell materials becomes available for numerical calibration and validation [23].

The application of the present extended model to many-particle systems (bulk behavior) is the final long-term goal, see Ref. [30] as an example, where the non-contact forces were disregarded. An interesting question that remains unanswered concerns a suitable analogy to the coefficient of restitution (as defined for pair collisions) relevant in the case of bulk systems, where particles can be permanently in contact with each other over long periods of time, and where impacts are not the dominant mode of interaction.

The interest of widely different communities viz. granular physics, particle technology, interstellar dust, asphalt or cold-spray in the dependence of restitution coefficient/deposition efficiency on impact velocity is considerable. We hope our study helps to connect these widely different communities by providing an overview and in particular a flexible multi-purpose contact model valid in many practically relevant situations.

## **6 Acknowledgment**

Insightful discussions with H. Tanaka, J. Tomas, O. Walton, C. Thornton, S. Li, M. Ghadiri, N. Kumar, S. Thakur and T. Weinhart are appreciated.

Financial support (project number: 07CJR06) from a research program “Jamming and Rheology” of the Stichting voor Fundamenteel Onderzoek der Materie (FOM), which is financially supported by the “Nederlandse Organisatie voor Wetenschappelijk Onderzoek” (NWO), is acknowledged.

## **A Energy Picture**

This appendix shows the energies of two particles during contact, where the difference between the different branches of the contact model, namely irreversible/unstable or

reversible/elastic, will be highlighted.

In Fig. 16, the time-evolution of kinetic and potential energy is shown; the graphs can be viewed in parallel to Figs. 9(a) and 9(b). In Fig. 16(a), we plot the kinetic and potential energy of the particles against time for low initial velocity  $\chi < \chi_c^{(1)}$ , corresponding to Fig. 9(a), for which dissipation is so weak that particles do not stick. The kinetic energy decreases from its initial value and is converted to potential energy (the conversion is complete at  $\delta_{\max}$ ). Thereafter, the potential energy drops due to the change between the loading and unloading slope from  $k_1$  to  $k_2$ . The potential energy decreases to zero (at the force-free overlap  $\delta_0$ ), where it is converted to (less) kinetic energy. Then the kinetic energy decreases further due to the acting adhesive force. At  $\delta_{\min}$  the increasing potential energy drops to a negative value due to the change in unloading slope from  $k_2$  to the adhesive (instable) slope  $-k_c$ . From there it increases from this minimum, negative value to zero, for  $\delta = 0$ . From here the kinetic energy remains constant and the potential energy stays at zero, since the particles are separated.

In Fig. 16(b), we plot the time evolution of kinetic and potential energy that the particles would have if un-/re-loading would take place at that moment, along the branch with slope  $k_2$ , namely the available (elastic) potential energy. This energy increases from zero at  $t = 0$ , and reaches a maximum when the kinetic energy becomes zero (note that it is not equal to the initial kinetic energy due to the plastic change of slope of  $k_2$ .) Thereafter, the available potential energy decreases to zero at the force-free overlap  $\delta_0$ . For further unloading, the available potential energy first increases and then drops rapidly on the unstable branch with slope  $-k_c$ . The change in sign of the unloading slope, from  $k_2$  to  $-k_c$ , is reflected in the kink in the curve at  $\delta_{\min}$ . Note, that comparing Figs. 16(a) and 16(b), the available potential energy always stays positive, while the total, plastic “potential” energy drops to negative values after the kink at  $\delta_{\min}$ .

Figs. 16(c) and 16(d) show the time evolution of kinetic and potential energy (total and available, respectively) for an initial velocity  $\chi_c^{(1)} < \chi < \chi_c^{(2)}$  in the sticking regime,

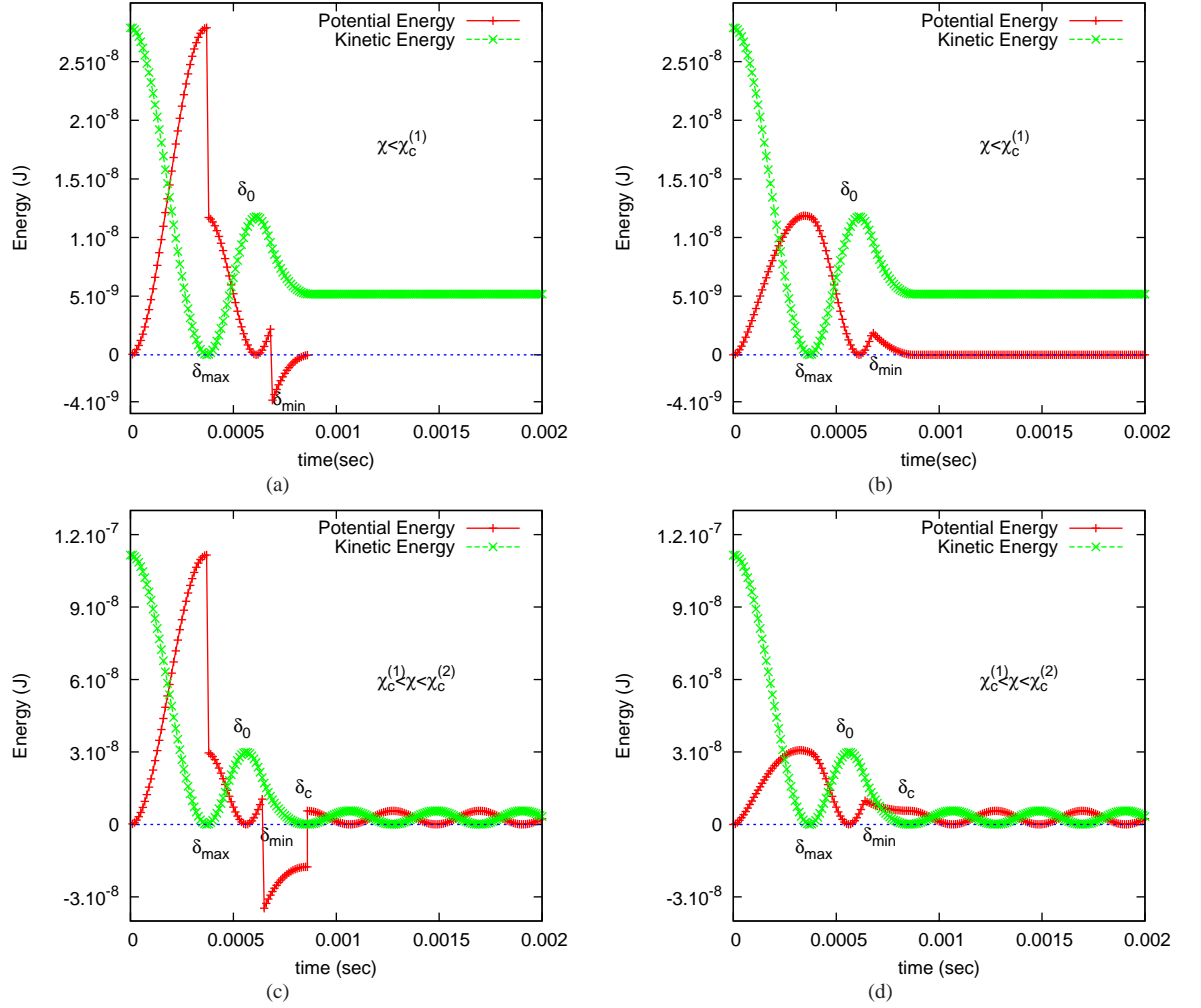


Figure 16: (a,c) Kinetic and (irreversible, plastic, “potential”) energy of the particles, and (b,d) kinetic and available (elastic) potential energy (for re-loading) of the particles, plotted against time for pair collisions with  $k_1 = 10^2 \text{ Nm}^{-1}$ ,  $k_p = 5 \times 10^2 \text{ Nm}^{-1}$ , and  $k_c = 10^2 \text{ Nm}^{-1}$ , i.e.  $\eta = 4$  and  $\beta = 1$ . The initial velocity  $\chi$  is  $\chi = 0.34$  (a,b) and  $\chi = 0.69$  (c,d), in the regimes defined in the inset of each plot.

see Fig. 9(b). In Fig. 16(c), a similar trend as that of Fig. 16(a) is observed until the potential energy becomes negative at  $\delta_{\min}$ . The difference to the case of smaller impact velocity is that at this point, the kinetic energy is less than the magnitude of the negative potential energy and hence first reaches zero, i.e., the particles stick. At this point, the (plastic) potential energy increases and jumps to a positive value indicating the change in sign of the unloading slope from  $-k_c$  to  $k_2$ . Finally, it oscillates between this positive value at  $\delta_c$ , exchanging energy with the kinetic degree of freedom. When the available potential energy is plotted in Fig. 16(d), a similar trend as that of Fig. 16(b) is observed up to the kink at  $\delta_{\min}$ . Here, the two energies have comparable values when they reach  $\delta_{\min}$  and the kinetic energy decreases to zero with a non-zero available potential energy, which causes the contact to re- and un-load along  $k_2$ .

## B Tuning of parameters to increase the plastic range

We assume that the reference dimensionless plasticity depth be  $\phi_f$ , which is e.g. calculated based on the maximal volume fraction related arguments of a multi-particle assembly, and  $k_p$  be the reference limit stiffness. We propose a new  $\phi_f' > \phi_f$  which represents the new dimensionless plasticity depth (our choice or calculated based on another volume fraction) and a new value of  $k_p'$  such that the tuned model resembles the reference for  $\delta_0 < a_{12}\phi_f$  and becomes plastic for  $a_{12}\phi_f < \delta_0 < a_{12}\phi_f'$ . At  $\delta_0 = a_{12}\phi_f$ , with  $a_{12}$  being reduced radius, Eq. (12) reads

$$k_p = k_2 = k_1 + (k_p' - k_1)\delta_{\max}^p / \delta_{\max}^p', \quad (\text{B.1})$$

since all parameters except  $\phi_f$  and  $k_p$  remain unchanged. Using this definition in Eq. (12) we arrive at

$$\frac{(k_p - k_1)^2}{k_p \phi_f} = \frac{(k_p' - k_1)^2}{k_p' \phi_f'}, \quad (\text{B.2})$$

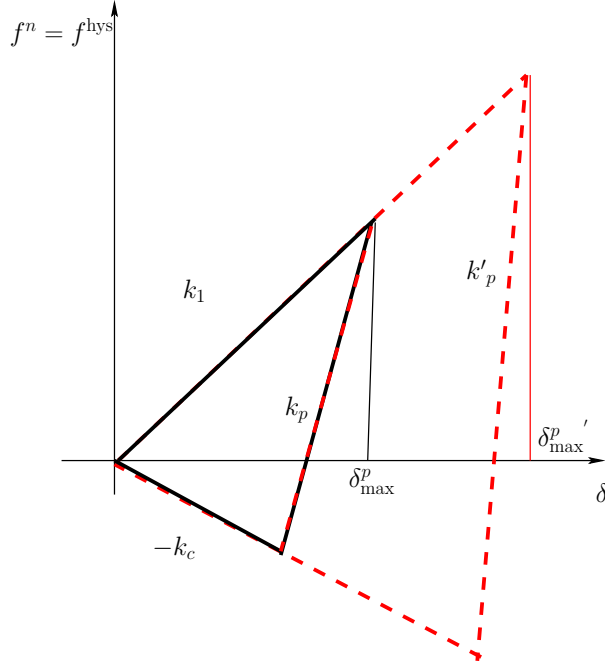


Figure 17: Force-displacement law for elasto-plastic, adhesive contacts superimposed on the irreversible contact force law. The black solid line represents the force law for reference input parameters  $\phi_f$  and  $k_p$ , while the dashed red line represents the same for a new chosen  $\phi_f'$  and newly calculated  $k_p'$  resembling a wider plastic regime of the particle deformation.

which gives the new limit stiffness

$$k_p' = \frac{2k_1 + AB + \sqrt{(AB)^2 + 4k_1AB}}{2}, \quad (\text{B.3})$$

where  $A = \frac{(k_p - k_1)^2}{k_p}$  and  $B = \frac{\phi_f'}{\phi_f}$ .

Using Eq. (B.3), we can calculate values of the new limit plastic stiffness  $k_p'$  for any given  $\phi_f'$ , such that the collision dynamics for lower plastic deformation  $\delta_0 < \delta_0^p$  is intact, while the range of plastic deformation is enhanced, depending on the chosen  $\phi_f' > \phi_f$ .

## C Agglomerate compression and tension test

Goal of this appendix is to show the unloading and re-loading behavior of an agglomerate, i.e. its effective, mesoscopic force-displacement relation, which clearly is different from the contact force law applied at the primary particle contacts. We will report incomplete detachment and partly/weaker elastic response for re-loading after various different compressive and tensile loading amplitudes.

The system considered here is an agglomerate (cubic) of size  $L_0 = 0.115$ , made of  $N = 1728$  primary particles of diameter  $d_0 = 0.01$  (with some variation in size to avoid monodisperse artefacts), just like in Ref. [29]. The cubic sample was first compressed (pressure-sintered) with a dimensionless wall stress  $d_0 p_s / k_p = 0.02$  to form a stable, rather dense agglomerate or “tablet”. The stress is first released to a value  $2 \cdot 10^{-5}$ , i.e.  $p_r / p_s = 10^{-3}$  for all walls. Then various uni-axial, unconfined tension/compression tests are carried out applying either further tension or compression starting from the released state of the sample [29]. The simulation parameters are same as in Ref. [29] (table 2), except for the cohesion that is set here to a rather small intensity,  $k_c / k_p = 0.2$ , rolling and sliding friction coefficients that are double as large,  $\mu_r = \mu_o = 0.2$ , and viscous damping of those degrees of freedom,  $\gamma_r / \gamma = \gamma_o / \gamma = 0.1$ , which also is larger than that of the reference situation.

The force-displacement curves for the tests at different amplitudes are shown in Figs. 18 and 20 for tension and compression tests respectively. All simulations in Figs. 18 and 20 start from the same configuration, i.e. the released state mentioned above and is indicated by the black circle at point (0,0). These plots represent the mesoscopic contact model of agglomerates consisting of multiple primary particles and their geometrical surface configurations and change in shape during the tests.

Fig. 18 shows the force-displacement curve for an unconfined uniaxial tension test. The black arrow shows the unloading/tension path, and finally arrows with different colors show the re-loading paths for different deformation amplitudes, as given in the

inset. Each of the tests, when it reaches the original strain at zero, is then repeated for three more cycles. Note that repeated cyclic loading remains on the same branch with positive slope, displaying the elastic nature of the contact, while it is *not* completely, perfectly detached. The contact surface is changing plastically by restructuring of the primary particles and surely is not flat, see Fig. 19, as one would expect for ideal, homogeneous, plastic materials. For the largest amplitude, the behavior is not perfectly elastic anymore, since the first plastic effects show up. For deformations as large as 0.2 of the primary particle diameter,  $d_0$ , before re-loading (arrow with positive slope on the red curve) has mostly, but not completely lost mechanical contact. The complete detachment of the assembly happens for much higher amplitude, than what is expected from a 2 particle interaction. Note that the contact model of the primary particles is behaving elasto-plastically ( $\phi_f = 0.05$ ) on the scale of only  $0.05d_0$ ; the reversible, elastic un-/re-loading is thus *not* due to the primary particle contact model, since it stretches to four times  $\phi_f d_0$  and even higher displacements. Finally, in order to confirm that this is not an effect of viscosity, qualitatively, the thick lines are simulations performed four times slower than those with thin lines.

In Fig. 19, a few snapshots during the tensile deformation are presented. The first snapshot corresponds to the undisturbed sample, while the others are increasing tensile deformation amplitudes. Note that these deformations are much larger than in Fig. 18. The contact is completely lost only at the extreme, final deformation in Fig. 19(g). In Fig. 19, it is also visible that the contact surface has developed a roughness of the size of several primary particles; the first visible gap is opened at a total deformation of  $D_x \sim d_0$ , and the contact is lost only at  $D_x \sim 8d_0$ , when the last of the thin threads breaks. The elastic, irreversible tension branch, however, is strongly developed only for much smaller  $D_x \sim d_0/5$ .

Complementing the tension test above, Fig. 20 shows the behavior of the same sample during compression cycles. The values given in the inset indicate the amplitude of



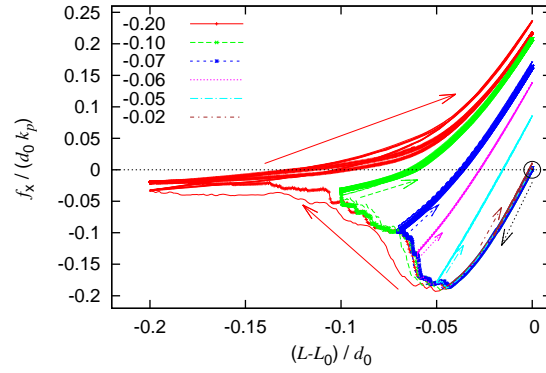


Figure 18: Dimensionless force-displacement curve for an unconfined uni-axial tension test (negative horizontal axis), with the various different deformation amplitudes  $D_x$  given in the inset. The downward arrow indicates the direction of first tensile unloading, while the upwards-right arrows indicate the change of force during re-loading. Except for the red curve, all these branches are reversible, for repeated un-/re-loading.

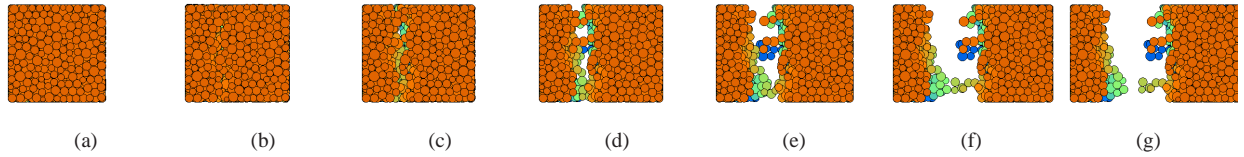


Figure 19: Snapshots of the tablet-sample during (large) tensile deformations for  $D_x = (L - L_0)/d_0 = 0$  (a), 0.81 (b), 1.8 (c), 3.1 (d), 4.7 (e), 7.4 (f), and 8.6 (g). The primary particles are colored according to their distance from the viewer (red, green, blue is increasing distance).

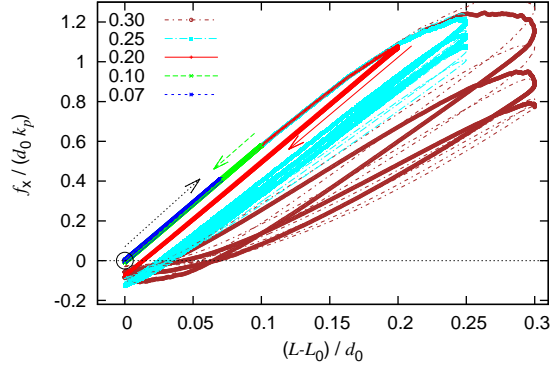


Figure 20: Dimensionless force-displacement curve for the same sample as in Fig. 18, but under compressive initial loading and un-/re-loading. The values in the inset indicate the maximal amplitudes  $D_x$ .

un-/re-loading. The smallest amplitudes remain elastic throughout, while plastic deformation kicks in for  $D_x > 0.1$  (see the red curve). However, the unloading and re-loading take place on the same branch, i.e. a new elastic branch (e.g. for  $D_x = 0.2$ ). For even larger amplitudes, e.g. the yellow curve with  $D_x = 0.3$ , the continuous damage/plastic destruction of the sample (by considerable irreversible re-arrangement during each cycle). Again, thick lines indicate simulations four times slower, which shows a small quantitative difference, but qualitative agreement even for the largest amplitude/rate. The snapshots in Fig. 21 show the continuous plastic deformation of the sample at large strains.

## References

- [1] M. P. Allen and D. J. Tildesley. *Computer Simulation of Liquids*. Oxford University Press, Oxford, 1987.
- [2] Y. M. Bashir and J. D. Goddard. A novel simulation method for the quasi-static mechanics of granular assemblages. *Journal of Rheology*, 35(5):849–885, 1991.

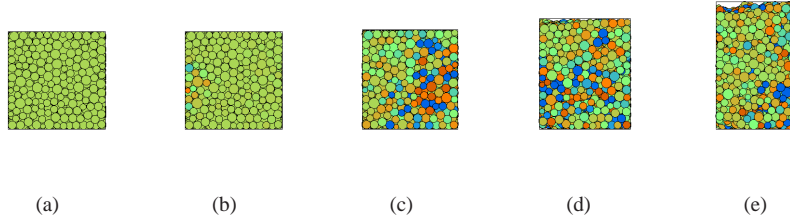


Figure 21: Snapshots of the tablet sample during compression at (large) deformations  $D_x = (L - L_0)/d_0 = 0$  (a), 0.01 (b), 0.3 (c), 0.8 (d), and 1.8 (e). The color code is small stress (green) and compressive/tensile larger stress (red/blue) averaged/isotropically per primary particle.

- [3] L. Brendel, J. Török, R. Kirsch, and U. Bröckel. A contact model for the yielding of caked granular materials. *Granular Matter*, 13(6):777–786, 2011.
- [4] N. V. Brilliantov, N. Albers, F. Spahn, and T. Pöschel. Collision dynamics of granular particles with adhesion. *Physical Review E*, 76:051302, 2007.
- [5] N. V. Brilliantov and T. Pöschel. *Collision of Adhesive Viscoelastic Particles*. Wiley VCH, 2005.
- [6] N. V. Brilliantov, F. Spahn, J. M. Hertzsch, and T. Pöschel. Model for collisions in granular gases. *Physical Review E*, 53(5):5382, 1996.
- [7] P. A. Cundall and O. D. L. Strack. A discrete numerical model for granular assemblies. *Géotechnique*, 29(1):47–65, 1979.
- [8] B. Dahneke. The influence of flattening on the adhesion of particles. *Journal of Colloid and Interface Science*, 40(1):1 – 13, 1972.
- [9] B. Dahneke. Measurements of bouncing of small latex spheres. *Journal of Colloid and Interface Science*, 45(3):584 – 590, 1973.
- [10] B. Dahneke. Further measurements of the bouncing of small latex spheres. *Journal of Colloid and Interface Science*, 51(1):58 – 65, 1975.

- [11] B. Derjaguin, V. Muller, and Y. P. Toporov. Effect of contact deformations on the adhesion of particles. *Journal of Colloid and interface science*, 53(2):314–326, 1975.
- [12] G. Haiat, M. P. Huy, and E. Barthel. The adhesive contact of viscoelastic spheres. *Journal of the Mechanics and Physics of Solids*, 51(1):69 – 99, 2003.
- [13] A. P. Hatzes, F. Bridges, D. N. C. Lin, and S. Sachtjen. Coagulation of particles in saturn’s rings: Measurements of the cohesive force of water frost. *Icarus*, 89(1):113 – 121, 1991.
- [14] S. Herminghaus. Dynamics of wet granular matter. *Advances in Physics*, 54(3):221–261, 2005.
- [15] H. J. Herrmann, J.-P. Hovi, and S. Luding, editors. *Physics of dry granular media - NATO ASI Series E 350*, Dordrecht, 1998. Kluwer Academic Publishers.
- [16] R. Jasevičius, R. Kačianauskas, and J. Tomas. Simulation of normal impact of micron-sized particle with elastic-plastic contact. *Journal of Vibroengineering*, 11(1):6–16, 2009.
- [17] R. Jasevičius, J. Tomas, and R. Kačianauskas. Simulation of normal impact of ultrafine silica particle on substrate. *Particulate Science and Technology*, 29(2):107–126, 2011.
- [18] M. Jiang, Y. Sun, L. Li, and H. Zhu. Contact behavior of idealized granules bonded in two different interparticle distances: An experimental investigation. *Mechanics of Materials*, 55:1 – 15, 2012.
- [19] M. Jiang, W. Zhang, Y. Sun, and S. Utili. An investigation on loose cemented granular materials via dem analyses. *Granular Matter*, 15(1):65–84, 2013.
- [20] K. L. Johnson. *Contact Mechanics*. Cambridge Univ. Press, Cambridge, 1985.

- [21] K. L. Johnson, K. Kendall, and A. D. Roberts. Surface energy and the contact of elastic solids. *Proceedings of Royal Society London A*, 324(1558):301–313, 1971.
- [22] L. Kempton, D. Pinson, S. Chew, P. Zulli, and A. Yu. Simulation of macroscopic deformation using a sub-particle DEM approach. *Powder Technology*, 223:19 – 26, 2012.
- [23] S. Kothe, J. Blum, R. Weidling, and C. Güttler. Free collisions in a microgravity many-particle experiment. III: The collision behavior of sub-millimeter-sized dust aggregates. *Icarus*, 225(1):75–85, 2013.
- [24] G. Kuwabara and K. Kono. Restitution coefficient in a collision between two spheres. *Japanese Journal of Applied Physics*, 26(8):1230–1233, 1987.
- [25] M. Lätzel, S. Luding, H. J. Herrmann, D. W. Howell, and R. P. Behringer. Comparing simulation and experiment of a 2d granular couette shear device. *The European Physical Journal E*, 11(4):325–333, 2003.
- [26] S. Li, J. S. Marshall, G. Liu, and Q. Yao. Adhesive particulate flow: The discrete-element method and its application in energy and environmental engineering. *Progress in Energy and Combustion Science*, 37(6):633 – 668, 2011.
- [27] S. Luding. Collisions & contacts between two particles. In H. J. Herrmann, J.-P. Hovi, and S. Luding, editors, *Physics of dry granular media - NATO ASI Series E350*, page 285, Dordrecht, 1998. Kluwer Academic Publishers.
- [28] S. Luding. Particulate solids modeling with discrete element methods. In P. Mas-saci, G. Bonifazi, and S. Serranti, editors, *CHoPS-05 CD Proceedings*, pages 1–10, Tel Aviv, 2006. ORTRA.
- [29] S. Luding. Cohesive, frictional powders: contact models for tension. *Granular Matter*, 10:235–246, 2008.

- [30] S. Luding and F. Alonso-Marroquín. The critical-state yield stress (termination locus) of adhesive powders from a single numerical experiment. *Granular Matter*, 13:109–119, 2011.
- [31] S. Luding, E. Clément, A. Blumen, J. Rajchenbach, and J. Duran. Anomalous energy dissipation in molecular dynamics simulations of grains: The “detachment effect”. *Physical Review E*, 50:4113, 1994.
- [32] S. Luding, E. Clément, A. Blumen, J. Rajchenbach, and J. Duran. Interaction laws and the detachment effect in granular media. In *Fractal Aspects of Materials*, volume 367, pages 495–500, Pittsburgh, Pennsylvania, 1995. Materials Research Society, Symposium Proceedings.
- [33] S. Luding and H. Herrmann. Micro-macro transition for cohesive granular media. *Zur Beschreibung komplexen Materialverhaltens, Institut für Mechanik, S. Diebels (Ed.), Stuttgart*, pages 121–133, 2001.
- [34] S. Luding, K. Manetsberger, and J. Müllers. A discrete model for long time sintering. *Journal of the Mechanics and Physics of Solids*, 53(2):455–491, 2005.
- [35] O. Molerus. Theory of yield of cohesive powders. *Powder Technology*, 12(3):259–275, 1975.
- [36] O. Molerus. Effect of interparticle cohesive forces on the flow behaviour of powders. *Powder Technology*, 20:161–175, 1978.
- [37] A. Moridi, S. Hassani-Gangaraj, and M. Guagliano. A hybrid approach to determine critical and erosion velocities in the cold spray process. *Applied Surface Science*, 273:617–624, 2013.
- [38] J. Morrissey, S. Thakur, J. Sun, J. Chen, and J. Ooi. Particle scale modelling of frictional cohesive granular materials. page 5, 2011.

- [39] T. Ormel, V. Magnanimo, H. t. Huerne, and S. Luding. Modeling of asphalt and experiments with a discrete particles method. In *Conference Proceedings MAIREPAV7 2012*, 2012.
- [40] A.-S. Persson and G. Frenning. An experimental evaluation of the accuracy to simulate granule bed compression using the discrete element method. *Powder Technology*, 219:249 – 256, 2012.
- [41] T. Pöschel and T. Schwager. *Computational Granular Dynamics - Models and Algorithms*. Springer, Berlin, Heidelberg, New York, 2005.
- [42] D. C. Rapaport. *The Art of Molecular Dynamics Simulation*. Cambridge University Press, Cambridge, 1995.
- [43] T. Schmidt, F. Gärtner, H. Assadi, and H. Kreye. Development of a generalized parameter window for cold spray deposition. *Acta Materialia*, 54(3):729–742, 2006.
- [44] C. Sorace, M. Louge, M. Crozier, and V. Law. High apparent adhesion energy in the breakdown of normal restitution for binary impacts of small spheres at low speed. *Mechanics Research Communications*, 36(3):364 – 368, 2009.
- [45] H. Tanaka, K. Wada, T. Suyama, and S. Okuzumi. Growth of cosmic dust aggregates and reexamination of particle interaction models. *Progress of Theoretical Physics Supplement*, 195:101–113, 2012.
- [46] S. Thakur, J. Ooi, and H. Ahmadian. Scaling of discrete element model parameter in uniaxial test simulation. In *The 6th International conference on discrete element methods, Golden, Colorado, USA.*, 2013.
- [47] S. C. Thakur, H. Ahmadian, J. Sun, and J. Y. Ooi. An experimental and numerical study of packing, compression, and caking behaviour of detergent powders. *Particuology*, 12:2–12, 2014.

- [48] S. C. Thakur, J. Sun, J. Y. Ooi, and H. Ahmadian. An experimental and numerical study of compression and shear behaviour of detergent powders. In *7th International Conference on Conveying and Handling of Particulate Solids*, 2012.
- [49] C. Thornton. Numerical simulations of deviatoric shear deformation of granular media. *Géotechnique*, 50(1):43–53, 2000.
- [50] C. Thornton, S. J. Cummins, and P. W. Cleary. An investigation of the comparative behaviour of alternative contact force models during elastic collisions. *Powder Technology*, 210(3):189 – 197, 2011.
- [51] C. Thornton, S. J. Cummins, and P. W. Cleary. An investigation of the comparative behaviour of alternative contact force models during inelastic collisions. *Powder Technology*, 233(0):30 – 46, 2013.
- [52] C. Thornton and Z. Ning. A theoretical model for the stick/bounce behaviour of adhesive, elastic-plastic spheres. *Powder technology*, 99(2):154–162, 1998.
- [53] C. Thornton and K. K. Yin. Impact of elastic spheres with and without adhesion. *Powder Technol.*, 65:153, 1991.
- [54] C. Thornton and L. Zhang. A DEM comparison of different shear testing devices. In Y. Kishino, editor, *Powders & Grains 2001*, pages 183–190, Rotterdam, 2001. Balkema.
- [55] J. Tomas. Particle adhesion fundamentals and bulk powder consolidation. *KONA Powder and Particle Journal*, 18:157–169, 2000.
- [56] J. Tomas. Assessment of mechanical properties of cohesive particulate solids. part 1: Particle contact constitutive model. *Particulate Science and Technology: An International Journal*, 19:95–110, 2001.



- [57] J. Tomas. Assessment of mechanical properties of cohesive particulate solids. part 2: Powder flow criteria. *Particulate Science and Technology: An International Journal*, 19:111–129, 2001.
- [58] J. Tomas. Adhesion of ultrafine particles – a micromechanical approach. *Chemical Engineering Science*, 62(7):1997 – 2010, 2007.
- [59] J. Tomas and S. Kleinschmidt. Improvement of flowability of fine cohesive powders by flow additives. *Chemical Engineering and Technology*, 32(10):1470–1483, 2009.
- [60] T. Van Steenkiste, J. Smith, R. Teets, J. Moleski, D. Gorkiewicz, R. Tison, D. Marantz, K. Kowalsky, W. Riggs, P. Zajchowski, et al. Kinetic spray coatings. *Surface and Coatings Technology*, 111(1):62–71, 1999.
- [61] P. A. Vermeer, S. Diebels, W. Ehlers, H. J. Herrmann, S. Luding, and E. Ramm, editors. *Continuous and Discontinuous Modelling of Cohesive Frictional Materials*, Berlin, 2001. Springer. Lecture Notes in Physics 568.
- [62] L. Vu-Quoc and X. Zhang. An elastic contact force-displacement model in the normal direction: displacement-driven version. *Proceedings Royal Society London A*, 455:4013–4044, 1999.
- [63] S. Wall, W. John, H.-C. Wang, and S. L. Goren. Measurements of kinetic energy loss for particles impacting surfaces. *Aerosol Science and Technology*, 12(4):926–946, 1990.
- [64] O. Walton. Potential discrete element simulation applications ranging from airborne fines to pellet beds. In *International Conference On Environmental Systems*, volume 01, page 2329, 2004.
- [65] O. Walton. Review of adhesion fundamentals for micron-scale particles. *KONA Powder and Particle Journal Powder and Particle*, 26:129–141, 2008.

- [66] O. R. Walton. Numerical simulation of inelastic, frictional particle-particle interactions. In M. C. Roco, editor, *Particulate two-phase flow*, page 884, Boston, 1993. Butterworth-Heinemann.
- [67] O. R. Walton and R. L. Braun. Stress calculations for assemblies of inelastic spheres in uniform shear. *Acta Mechanica*, 63:73, 1986.
- [68] O. R. Walton and R. L. Braun. Viscosity, granular-temperature, and stress calculations for shearing assemblies of inelastic, frictional disks. *J. Rheol.*, 30(5):949–980, 1986.
- [69] O. R. Walton and S. M. Johnson. Simulating the effects of interparticle cohesion in micron-scale powders. *AIP Conference Proceedings*, 1145(1):897–900, 2009.
- [70] J. Wu, H. Fang, S. Yoon, H. Kim, and C. Lee. The rebound phenomenon in kinetic spraying deposition. *Scripta Materialia*, 54(4):665–669, 2006.
- [71] D. Zhang, P. Shipway, and D. McCartney. Cold gas dynamic spraying of aluminum: The role of substrate characteristics in deposit formation. *Journal of Thermal Spray Technology*, 14:109–116, 2005.
- [72] X. Zhang and L. Vu-Quoc. Simulation of chute flow of soybeans using an improved tangential force-displacement model. *Mechanics of Materials*, 32:115–129, 2000.
- [73] X. Zhang and L. Vu-Quoc. Modeling the dependence of the coefficient of restitution on the impact velocity in elasto-plastic collisions. *International Journal of Impact Engineering*, 27(3):317–341, 2002.
- [74] X. Zhou, X. Wu, J. Wang, J. Zhang, et al. Numerical investigation of the rebounding and the deposition behavior of particles during cold spraying. *Acta Metall. Sin.(English Lett.)*, 24(1):45–53, 2011.